

1 **Title: A genome-scale atlas reveals complex interplay of transcription and translation in**  
2 **an archaeon**

3

4 Authors: Alan P. R. Lorenzetti <sup>1,2</sup>, Ulrike Kusebauch <sup>2</sup>, Lívia S. Zaramela <sup>1</sup>, Wei-Ju Wu <sup>2</sup>, João P.  
5 P. de Almeida <sup>1,3</sup>, Serdar Turkarslan <sup>2</sup>, Adrián L. G. de Lomana <sup>2,4</sup>, José V. Gomes-Filho <sup>1,5</sup>,  
6 Ricardo Z. N. Vêncio <sup>6</sup>, Robert L. Moritz <sup>2</sup>, Tie Koide <sup>1,†</sup>, Nitin S. Baliga <sup>2,7,8,9,†,#</sup>

7

8 Affiliations:

9 <sup>1</sup> Department of Biochemistry and Immunology, Ribeirão Preto Medical School, University of São Paulo,  
10 Ribeirão Preto, Brazil

11 <sup>2</sup> Institute for Systems Biology, Seattle, WA, USA

12 <sup>3</sup> Present address: Institute of Biological Sciences, Federal University of Minas Gerais, Belo Horizonte,  
13 Brazil

14 <sup>4</sup> Present address: Center for Systems Biology, University of Iceland, Reykjavik, Iceland

15 <sup>5</sup> Present address: Prokaryotic RNA Biology, Phillips-Universität Marburg, Marburg, Germany

16 <sup>6</sup> Department of Computation and Mathematics, Faculty of Philosophy, Sciences and Letters at Ribeirão  
17 Preto, University of São Paulo, Ribeirão Preto, Brazil

18 <sup>7</sup> Departments of Biology and Microbiology, University of Washington, Seattle, WA, USA

19 <sup>8</sup> Molecular and Cellular Biology Program, University of Washington, Seattle, WA, USA

20 <sup>9</sup> Lawrence Berkeley National Lab, Berkeley, CA, USA

21 <sup>†</sup> TK and NSB are joint senior authors

22 <sup>#</sup> Author to whom correspondence should be addressed

23

24 E-mail: nitin.baliga@isbscience.org; Tel.: +1 (206) 732-1266

25

26 **ABSTRACT**

27 The scale of post-transcriptional regulation and the implications of its interplay with other forms of  
28 regulation on environmental acclimation is underexplored for organisms of the domain Archaea.  
29 Here, we have investigated the scale of post-transcriptional regulation in the extremely halophilic  
30 archaeon *Halobacterium salinarum* NRC-1 by integrating transcriptome-wide locations of  
31 transcript processing sites (TPS) and SmAP1 binding, genome-wide locations of antisense RNAs  
32 (asRNAs), and consequences of RNase\_2099C knockout on differential expression of all genes.  
33 This integrated analysis has discovered that 54% of all protein-coding genes in the genome of  
34 this haloarchaeon are likely targeted by multiple mechanisms for putative post-transcriptional  
35 processing and regulation, with about 20% of genes likely regulated by combinatorial schemes  
36 involving SmAP1, asRNAs, and RNase\_2099C. Comparative analysis of mRNA levels (RNA-  
37 Seq) and protein levels (SWATH-MS) for 2,579 genes over four phases of batch culture growth  
38 in complex medium has generated additional evidence for conditional post-transcriptional  
39 regulation of 7% of all protein-coding genes. We demonstrate that post-transcriptional regulation  
40 may act to fine-tune specialized and rapid acclimation to stressful environments, e.g., as a switch  
41 to turn on gas vesicle biogenesis to promote vertical relocation in anoxic conditions and to  
42 modulate frequency of transposition by IS elements of the IS200/IS605, IS4, and ISH3 families.  
43 Findings from this study are provided as an atlas in a public web resource  
44 (<https://halodata.systemsbiology.net>).

45 **IMPORTANCE** While the transcriptional regulation landscape of archaea has been extensively  
46 investigated, we currently have limited knowledge about post-transcriptional regulation and its  
47 driving mechanisms in this domain of life. In this study, we collected and integrated omics data  
48 from multiple sources and technologies to infer post-transcriptionally regulated genes and the  
49 putative mechanisms modulating their expression at the protein level in *Halobacterium salinarum*  
50 NRC-1. The results suggest that post-transcriptional regulation may drive environmental  
51 acclimation by regulating hallmark biological processes. To foster discoveries by other research  
52 groups interested in the topic, we extended our integrated data to the public in the form of an  
53 interactive atlas (<https://halodata.systemsbiology.net>).

54

55 **INTRODUCTION**

56 By virtue of their co-existence with multiple organisms within a community, microbes are under  
57 significant evolutionary selection pressure to maximize resource utilization for growth and  
58 sustenance, while minimizing waste (1). For this reason, even within their streamlined genomes,  
59 microbes possess extensive regulatory mechanisms at multiple levels of information processing  
60 (2–5). While regulation at the transcriptional level is typically modular with genome-wide  
61 consequences (4, 6), regulation at the post-transcriptional level is believed to be more nuanced  
62 and localized to specific sets of functions that are directly associated with environment-specific  
63 phenotypic traits (7). In other words, while transcriptional regulation mediates large-scale  
64 physiological adjustments, post-transcriptional regulation fine-tunes specific functions to optimize  
65 environmental acclimation. Understanding the interplay of regulation across the different layers  
66 of information processing will give insight into how microbes compete and collaborate effectively  
67 with other co-inhabiting organisms. In addition to having foundational significance, these insights  
68 also have important implications for synthetic biology approaches to introduce novel traits while  
69 minimizing fitness tradeoffs in an engineered organism (8–11).

70 Understanding the interplay of regulation across transcription and translation in organisms  
71 of the domain Archaea is especially interesting for several reasons. First, while they have been  
72 discovered across diverse environments, archaea are particularly known for specialized  
73 phenotypic adaptations for some of the most extreme and dynamic habitats (12). Second,  
74 archaea are unique in terms of possessing a mix of information processing mechanisms that are  
75 distinctly eukaryotic or bacterial. For instance, while their general transcriptional machinery  
76 including the RNA polymerase shares ancestry with eukaryotic counterparts, the regulation of  
77 transcription is mediated by regulators that have bacterial ancestry (13, 14). There has been  
78 extensive work across several archaeal model organisms that has characterized basal  
79 transcription and its regulation both in molecular detail and at a systems level (2, 3, 15). By  
80 contrast, it has been only in the recent past that we have begun to appreciate the role of post-  
81 transcriptional regulatory mechanisms in specialized phenotypic acclimation of archaea. There is  
82 evidence that translational efficiency in methanogenic archaea is modulated through differential  
83 processing of 5' UTRs (16), mRNA secondary structures (17), or context-specific binding by small  
84 regulatory RNAs (sRNAs) to conditionally occlude ribosome binding sites within transcripts (18)  
85 or to stabilize them (19). Studies conducted in a psychrophile have discovered that post-  
86 transcriptional regulation directly influences methanol conversion into methane at lower  
87 temperatures (20). Similarly, RNase-mediated disruption of positive autoregulation of potassium

88 uptake was discovered to be an important mechanism for energetically-efficient and rapid  
89 acclimation of a halophile in a salinity shift scenario (21). These examples illustrate how some  
90 archaea utilize post-transcriptional regulation to fine-tune specific functions and pathways for  
91 specialized phenotypic acclimation to environmental change.

92 However, a lot remains to be understood regarding the scale of post-transcriptional  
93 regulation in archaea and the extent to which they are deployed in combinatorial schemes to fine-  
94 tune phenotypes for environmental acclimation. For instance, the widely conserved and  
95 extensively characterized RNA-binding proteins (RBP), including Csp (A, C, and E), CsrA,  
96 RNaseE, YbeY, and Hfq, are known to play important post-transcriptional regulatory functions in  
97 bacteria (22), but there is limited understanding of the roles of their orthologs in archaea. Hfq is a  
98 member of an RNA-guided complex, a well-characterized bacterial RNA chaperone known to  
99 interfere in mRNA translation (23, 24), which acts in a manner analogous to the RNA-induced  
100 silencing complex (RISC) in eukaryotes to regulate specific mRNAs (25). Notably, the Hfq  
101 homolog, Sm-like archaeal protein (SmAP1 or Lsm), has been characterized structurally across  
102 multiple archaea (26–29), including *Halobacterium salinarum* NRC-1 (30), and shown to likely  
103 mediate post-transcriptional regulation through sRNA-binding in *Haloferax volcanii* (31, 32) and  
104 *Sulfolobus solfataricus* (33). However, we do not understand the mechanism, importance, context  
105 or scale of post-transcriptional regulation mediated by SmAP1 (and other RBPs) (34, 35) or, for  
106 that matter, by the large numbers of sRNAs, antisense RNAs (asRNAs), and RNases that have  
107 been discovered across archaeal genomes (36).

108 Here, we have investigated the scale of interplay between transcriptional and post-  
109 transcriptional mechanisms in regulating protein levels in the halophilic archaeon *H. salinarum*  
110 NRC-1, which has served as a model to investigate traits of organisms in the domain Archaea. In  
111 particular, *H. salinarum* NRC-1 has been widely used as a model organism to dissect hallmark  
112 traits of halophilic archaea, including niche adaptation via expanded families of general  
113 transcription factors (37), large-scale genome organization by genomic repeats and insertion  
114 sequences (IS) (38, 39), flotation by gas vesicle biogenesis (40), phototransduction by  
115 bacteriorhodopsin (41), and how modularity of translational complexes enables rapid acclimation  
116 to environmental changes (42). Prior work has characterized at a systems level and in  
117 mechanistic detail many aspects of the global transcriptional regulatory network of *H. salinarum*  
118 NRC-1 (2, 3), with extensive validations through genetic perturbation studies and physical  
119 mapping of genome-wide protein-DNA interactions of multiple transcription factors (4, 5).  
120 However, the transcriptional regulatory network by itself or the half-lives of all transcripts (43) did

121 not fully explain the complex relationship between absolute and relative abundance of transcripts  
122 and proteins across different environmental contexts (44, 45), suggesting an important role for  
123 post-transcriptional regulation. Indeed, prior studies have uncovered evidence for the potential of  
124 extensive post-transcriptional regulation in *H. salinarum* NRC-1, including the presence of a  
125 strikingly large number of regulatory elements within coding sequences (3) that leads to  
126 widespread conditional splitting of at least 40% of all operons into multiple overlapping  
127 transcriptional units (5), presence of asRNAs for 22% of all genes (46), differential regulation of  
128 23 transcripts in an RNase knockout background (21), and extensive transcript processing sites  
129 (TPS) across 43% of all coding sequences (47).

130 Through integrated analysis of a new transcriptome-wide map of SmAP1 binding located  
131 with RNA immunoprecipitation sequencing (RIP-Seq), global differential regulation of transcripts  
132 upon deletion of an RNase (VNG\_2099C) implicated in acclimation to salinity change (21), and  
133 locations of asRNAs and TPS (46, 47), we have generated a genome-scale atlas that has  
134 discovered that 54% of all protein-coding genes in *H. salinarum* NRC-1 are targeted by multiple  
135 mechanisms for putative post-transcriptional regulation. Interestingly, 20% of all protein-coding  
136 genes are likely post-transcriptionally regulated in combinatorial schemes involving SmAP1,  
137 asRNAs, and RNase. Further, through comparative analysis of dynamic changes in mRNA levels  
138 (RNA-Seq), ribosome footprints (Ribo-Seq) (42), and protein levels (SWATH-MS) (Kusebauch et  
139 al., in preparation) for 2,579 representative genes over four phases of batch culture growth in  
140 complex medium, we have generated evidence that 7% of all protein-coding genes (188 genes)  
141 are indeed post-transcriptionally regulated. Notably, 78% of these post-transcriptionally regulated  
142 genes were mechanistically associated with SmAP1-binding, asRNAs, TPS, and/or RNase-  
143 mediated differential regulation. Through in-depth analysis we demonstrate how post-  
144 transcriptional regulation acts to fine-tune specialized environmental acclimation, e.g., as a switch  
145 to turn on gas vesicle biogenesis and to modulate frequency of transposition by IS elements of  
146 the IS200/IS605, IS4, and ISH3 families. Finally, we have generated an interactive web resource  
147 to support collaborative community-wide exploration and characterization of the *H. salinarum*  
148 NRC-1 multi-omics Atlas (<https://halodata.systemsbiology.net>).

149 **RESULTS**

150 *Evidence for post-transcriptional regulation by SmAP1, asRNAs, and RNase\_2099C*

151 Since the publication of its genome sequence in 2000, multiple sources of gene annotations have  
152 emerged for *H. salinarum* NRC-1 (48–50). To standardize annotations, we clustered sequences  
153 from each source to eliminate redundancy while differentiating between paralogs (see Methods;  
154 Table S1; File S1). In summary, this analysis identified 2,631 non-redundant transcripts, including  
155 2,579 coding and 52 non-coding RNAs (rRNAs, tRNAs, signal recognition particle RNA, and  
156 RNase P) with a dictionary anchored by locus tags from (50) and mapped to locus tags of the  
157 closely related strain *H. salinarum* R1 (File S1).

158 Next, we compiled orthogonal, genome-wide evidence for putative post-transcriptional  
159 regulation. Specifically, we relocated one or more published transcript processing sites (TPS)  
160 within at least 966 protein-coding genes (37% of all protein-coding genes) (47), mapped cis-acting  
161 asRNAs for 536 genes (46), and determined that 166 genes were differentially expressed upon  
162 deletion of one out of 12 RNases predicted within the genome (VNG\_2099C; here onwards  
163 “RNase\_2099C”) (21) (File S2). To characterize the role of SmAP1 (VNG\_1496G) in *H. salinarum*  
164 NRC-1, epitope-tagged SmAP1-RNA complexes were co-immunoprecipitated from late-  
165 exponential phase cultures from standard growth conditions (Figure S1), and transcriptome-wide  
166 binding locations of SmAP1 were mapped by enrichment of sequenced transcripts (RIP-Seq; see  
167 Methods). Consistent with previous *in vitro* observations from diverse archaea, the RIP-Seq  
168 analysis discovered that SmAP1 preferentially binds to AU-rich transcripts (Figure S2A) (28–31,  
169 51). In particular, we determined that SmAP1 binds to 15% (397/2,579) of all protein-coding  
170 transcripts in *H. salinarum* NRC-1, including its own coding transcript (File S1), suggesting  
171 putative autoregulation in light of the observed dynamics for mRNA and protein levels (Figure  
172 S2B).

173 Integrated analysis of locations of SmAP1 binding, asRNAs, and TPS, and differential  
174 expression in  $\Delta$ RNase\_2099C revealed that at least 1,394 genes were potentially subject to post-  
175 transcriptional regulation by at least one of these mechanisms, with 514 genes under putative  
176 combinatorial regulation by two or more mechanisms (Figure 1). Interestingly, transcripts that  
177 were upregulated in the  $\Delta$ RNase\_2099C strain background were preferentially bound by SmAP1  
178 ( $p$ -value = 0.02), associated with cognate asRNAs ( $p$ -value = 0.04), and enriched for TPS ( $p$ -  
179 value =  $6.7 \times 10^{-5}$ ). These findings could suggest that SmAP1 and asRNAs are responsible for the  
180 recruitment of RNase\_2099C to mediate targeted cleavage of transcripts. Thus, the integrated  
181 analysis predicted that 20% to 54% of the *H. salinarum* genome is post-transcriptionally regulated

182 (Figure 1; 514 to 1,394 out of 2,579 genes). The fact that SmAP1, asRNAs, and RNase\_2099C  
183 account for putative regulation of 858 genes, suggests that myriad mechanisms, potentially  
184 involving other RBPs and RNases noted above, are likely at play even in the limited conditions  
185 represented in standard growth conditions.

186

187 *Evidence of post-transcriptional regulation in global trends of mRNA and protein levels*

188 We investigated concordance in patterns of absolute abundance at the transcriptional and  
189 translational levels for each gene by calculating Pearson correlation coefficients between mRNA  
190 and protein quantification across all the sampled physiological states ( $R_{TP1} = 0.67$ ;  $R_{TP2} = 0.68$ ;  
191  $R_{TP3} = 0.57$ ;  $R_{TP4} = 0.44$ ) (Figure 2A-D). The weaker correlation ( $R_{TP1} = R_{TP2} > R_{TP3} > R_{TP4}$ ; Table  
192 S2) in later stages of batch culture growth was skewed towards repression of translation; that is,  
193 highly abundant mRNAs were associated with low abundance proteins in the quiescent  
194 physiological state (TP4). We also noticed that protein levels correlated slightly better with mRNA  
195 levels from the previous time point ( $R_{P-TP2\text{ m-TP1}} = 0.68$ ;  $R_{P-TP3\text{ m-TP2}} = 0.67$ ;  $R_{P-TP4\text{ m-TP3}} = 0.57$ ; Figure  
196 2E-G; Table S2), which is consistent with the sequential and temporal relationship between  
197 transcription and translation, as we have previously shown (44, 45). We discovered that 6.5% of  
198 all protein-coding genes (167) with high mRNA levels (upper quintile) were associated with low  
199 protein levels (lower quintile or undetected) over some or all four stages of growth in batch culture  
200 (Figure S3A, File S3). Specifically, the 167 genes were enriched for SmAP1 binding, asRNAs,  
201 and TPS ( $p$ -value =  $2.3 \times 10^{-4}$ ,  $2.9 \times 10^{-2}$ , and  $1.1 \times 10^{-7}$ , respectively) and had longer average mRNA  
202 half-lives (13.7 min. vs. 12.3 min.;  $p$ -value =  $1.1 \times 10^{-2}$ ). Within this set, 64 genes associated with  
203 protein levels detected in the lower quintile (green points in Figure 2A-D; Figure S3B; File S3)  
204 were enriched for TPS ( $p$ -value =  $2.6 \times 10^{-4}$ ). A second set of 117 genes, whose proteins were not  
205 detected likely due to their low levels or complete absence (see Methods; Figure S3C; File S3),  
206 was enriched for SmAP1 binding and TPS ( $p$ -value =  $1.7 \times 10^{-6}$  and  $2.8 \times 10^{-6}$ , respectively), had  
207 longer average mRNA half-lives (14.2 min. vs. 12.3 min;  $p$ -value =  $2.7 \times 10^{-3}$ ), and was upregulated  
208 in  $\Delta RNase\_2099C$  strain ( $p$ -value =  $1.5 \times 10^{-2}$ ). Refer to File S4 for sets and tests.

209 Finally, we searched for potentially post-transcriptionally regulated genes by correlating  
210 dynamic relative changes in protein and mRNA levels over time (Figure 2H-L; File S5; File S6).  
211 For example, during the transition from TP1 to TP2, we observed a decrease in protein abundance  
212 of five transcriptionally upregulated genes over the same timeframe (Figure 2H). This cluster  
213 (Figure S4; File S6), comprised of five genes depicted by green points (VNG\_7025, VNG\_7026,  
214 VNG\_7039, VNG\_7103, and VNG\_6313G) in Figure 2H, with enrichment for SmAP1 binding,

215 asRNAs, and TPS ( $p$ -value =  $8.5 \times 10^{-5}$ ,  $3.8 \times 10^{-4}$ , and 0, respectively), is a strong candidate for  
216 post-transcriptional repression. The genes also had lower codon adaptation index (CAI; 0.64 vs.  
217 0.77;  $p$ -value =  $3.9 \times 10^{-3}$ ) and increased mRNA levels in the  $\Delta RNase\_2099C$  strain ( $\log_2$  fold  
218 change = 1 vs. 0.02;  $p$ -value =  $3.5 \times 10^{-4}$ ). The comparative analysis of mRNA and protein  
219 abundance changes across all transition states (TP1 to TP2, TP2 to TP3, TP3 to TP4, TP1 to  
220 TP3 and TP1 to TP4) identified 26 potentially post-transcriptionally repressed transcripts (Figure  
221 S5; File S6) enriched for SmAP1 binding and TPS ( $p$ -value =  $3.5 \times 10^{-3}$  and  $2.3 \times 10^{-4}$ , respectively),  
222 and upregulated in  $\Delta RNase\_2099C$  strain ( $p$ -value =  $9.2 \times 10^{-7}$ ). Again, refer to File S4 for sets and  
223 tests.

224 Altogether, the combined analyses of correlations between absolute and relative  
225 abundance of mRNAs and proteins provided further evidence for post-transcriptional regulation  
226 of at least 7% of all genes (188 out of 2,579) in *H. salinarum* NRC-1 during transition from active  
227 growth to the stationary phase. Notably, 78% of these genes (147/188) with poor mRNA-protein  
228 correlation were among the 1,394 genes associated with putative post-transcriptional regulation  
229 features, including SmAP1 binding, asRNAs, and TPS ( $p$ -value =  $1.9 \times 10^{-9}$ ,  $7.6 \times 10^{-6}$ , and  $2.5 \times 10^{-21}$ ,  
230 respectively). Together these findings suggest complex combinatorial post-transcriptional  
231 regulation of these genes at specific growth stages.

232

### 233 *Construction of the H. salinarum NRC-1 multi-omics Atlas*

234 To facilitate discovery of evidence of post-transcriptional regulation, we compiled corresponding  
235 quantitation of mRNAs (RNA-Seq), ribosome-protected mRNA fragments (RPF; Ribo-Seq) (42),  
236 and proteins (SWATH-MS) (Kusebauch et al., in preparation), quantile normalized them (File S1)  
237 for scale adjustment, and performed calculations of translational efficiency (TE) and ribosome  
238 occupancy (RO) for 2,579 genes across early exponential (TP1), mid-exponential (TP2), late-  
239 exponential (TP3), and stationary (TP4) phases of growth in batch culture (see Methods; Figure  
240 3; File S7). Further, we also included general properties such as GC content, mRNA half-life, and  
241 CAI for each gene, as they are known to influence dynamics of the interplay between transcription  
242 and translation (43, 52) and could likely explain discrepant patterns of corresponding changes  
243 across mRNA, RPF, and proteins. A quick exploratory analysis of GC content and CAI, brought  
244 up their association to protein levels in this study (Figure S6). Genes in the atlas were organized  
245 into nine groups based on patterns of absolute abundance (File S3) and relative changes across  
246 mRNA and protein levels (File S6). This analysis revealed that at least 188 genes (7% of all  
247 protein-coding genes in the atlas) had incoherent mRNA-protein correlation patterns across the

248 four physiological states during growth in batch culture. Notably, 147 of these 188 genes were  
249 associated with at least one post-transcriptional regulation mechanism noted above. The *H.*  
250 *salinarum* NRC-1 Atlas is accessible through an application (<https://halodata.systemsbiology.net>)  
251 that supports interactive exploration by zooming into specific segments of a heatmap, by  
252 searching for genes of interest, or through a searchable genome browser. The following sections  
253 demonstrate how the atlas facilitates in-depth investigations into post-transcriptional regulation of  
254 hallmark processes in *H. salinarum* NRC-1.

255

256 *Functional implications of growth-associated post-transcriptional regulation in H. salinarum*  
257 Altogether, the comparison of absolute and relative abundance of mRNA and protein levels  
258 yielded evidence for post-transcriptional regulation of 188 genes during batch culture growth  
259 (Figure 2; File S3; File S6). Furthermore, the longer transcript half-lives together with enrichment  
260 of SmAP1-binding, asRNAs, TPS, and differential regulation upon deletion of RNase\_2099C  
261 provided evidence for post-transcriptional processing, and associated putative mechanisms of  
262 regulation of different gene subsets. While a substantial number of genes were of unknown  
263 function, important processes were represented among genes of known functions; these included  
264 gas vesicle biogenesis, transposition-mediated genome reorganization, motility, translation, and  
265 energy transduction (Figure 4). Among these, both gas vesicles and extensive genome  
266 reorganization mediated by activity of mobile genetic elements are hallmark traits of *H. salinarum*  
267 NRC-1 that are triggered in specific environmental contexts, including late growth and stationary  
268 phases. Below, we present vignettes on each of these two processes to illustrate how the *H.*  
269 *salinarum* NRC-1 multi-omics Atlas enables the discovery of mechanistic insight into post-  
270 transcriptional regulation of specific phenotypes.

271 *The role of SmAP1 in the regulation of transposition and genome reorganization.*  
272 Transposases are typically encoded within insertion sequences (IS), a type of transposable  
273 element that is ubiquitous across prokaryotes, and known to mediate self-mobilization to new  
274 locations in the genome (53, 54). *H. salinarum* NRC-1 mobilome is comprised by 80 full and 33  
275 partial IS elements of eight families (ISfinder/ISbrowser) (55, 56), some of which are known to  
276 introduce phenotypic diversity in flotation, by disrupting *gvp* locus at 1-5% frequency, and also in  
277 phototrophic energy production, by disrupting the bacteriorhodopsin gene (*bop*) locus at 0.01%  
278 frequency, potentially driving niche acclimation in brine pools (38, 57, 58). Notably, SmAP1 bound  
279 24 of the 33 mobilome transcripts (Figure 5A; Figure S2C; enrichment *p*-value =  $10^{-14}$ ), consistent  
280 with their low GC content (Figure 5B) and the previously implicated role of its bacterial homolog

281 in regulating transposition events (59, 60). Out of the 33 mobilome proteins, only four were  
282 detected at the protein level (Figure 5AC), including three TnpB proteins encoded by IS elements  
283 of the IS200/IS605 family subgroup IS1341 (VNG\_0013C, VNG\_0044H, and VNG\_2652H) and  
284 one protein encoded by the multi-copy ISH2 element (VNG\_0210H), belonging to the ISH8 family  
285 (see Table S3 for IS information). All mobilome proteins, except for one (VNG\_0051a), were  
286 present in the SWATH-MS assay library and none were predicted to be membrane-associated.  
287 Moreover, all produced at least one suitable tryptic peptide ( $\geq 7$  and  $\leq 30$  amino acids) when  
288 digested *in silico* (Rapid Peptides Generator) (61). Notwithstanding their low CAI (Figure 5D), the  
289 high mRNA abundance (Figure 5E), and presence of TPS suggests that the mobilome proteins  
290 were not detected by virtue of being expressed at low abundance, and possibly due to post-  
291 transcriptional repression of translation by SmAP1 and asRNAs (Figure 5A). For instance, the  
292 translational repression of VNG\_0112H (ISH3 family) would be consistent with the observed pile-  
293 up of Ribo-Seq reads at the 5' end of the transcript, which is co-located with SmAP1 binding sites  
294 and a TPS (Figure S7). Together, these observations suggest SmAP1 binding might lead to a  
295 potentially stalled ribosome-transcript complex, which may then be targeted by an endonuclease  
296 in a well-known mechanism called “No-Go” decay, as previously hypothesized for similar  
297 observations (47). The evidence provided by the atlas offered confidence for further wet lab  
298 experimental exploration. Therefore, we investigated the role of SmAP1 in regulation of IS  
299 element-mediated genome reorganization by performing long-read DNA sequencing (DNA-Seq)  
300 to quantify transposition events of each IS family in  $\Delta$ ura3 $\Delta$ smap1 strain and its parent  $\Delta$ ura3  
301 (Figure 6; Figure S8; Table S4; File S8). In so doing, we discovered that knocking out SmAP1  
302 significantly decreased the overall number of transposition events (Figure 6A), and in particular  
303 transposition of the IS4 and ISH3 families (Figure 6B-C).

304 *The role of post-transcriptional regulation in governing environmental responsiveness and*  
305 *timing of gas vesicle biogenesis.* Gas vesicles are intracellular proteinaceous organelles filled with  
306 ambient gas that may be used as buoyancy devices by halophilic archaeal cells to float to the  
307 surface to access oxygen, which has poor solubility in hypersaline water (62). The gas vesicles  
308 also act in conjunction with sensory rhodopsin-mediated phototaxis to support phototrophic  
309 energy transduction by bacteriorhodopsin (63). Hence, the biogenesis of gas vesicles is highly  
310 responsive to environmental stimuli, and in particular oxygen availability (64). Gas vesicles are  
311 made up of two structural proteins: GvpA, a monomer, and GvpC, which wraps around and  
312 stabilizes the vesicle assembled from the GvpA polymer (65). Many other proteins (GvpF-M) are  
313 involved in nucleation and biogenesis of the gas vesicle (66), a process that is regulated by GvpD  
314 and GvpE (40). The bidimensional trajectories of changes in mRNA and protein levels revealed

315 that while the transcript levels of all *gvp* genes, including the structural proteins, increased across  
316 the four growth phases, the corresponding protein levels did not increase until the cells  
317 transitioned from mid-exponential growth phase into the stationary phase (Figure 7A), which is  
318 consistent with the timing of gas vesicle production (67). Together, the multiple levels of evidence  
319 in the *H. salinarum* NRC-1 Atlas (Figure 7B; Figure S9) supports a model (Figure 7C) that explains  
320 how the interplay of negative and positive regulation at the transcriptional, post-transcriptional,  
321 and translational levels governs the timing and environmental responsiveness of gas vesicle  
322 biogenesis.

323 Based on the absolute abundance and relative change in mRNA and protein levels, we  
324 posit that *gvp* genes were constitutively transcribed across all phases of growth. But translation  
325 of *gvp* transcripts required further transcriptional activation by GvpE (68), which was prevented in  
326 early and mid-exponential growth phase by GvpD. Specifically, in the early growth phase GvpD  
327 was high in abundance and above a threshold at which it drives the degradation of GvpE (69, 70)  
328 (Figure 7AC). As cells transitioned from early to mid-growth phase, SmAP1, RNase\_2099C, and  
329 asRNAs acted in concert to repress translation of *gvp* transcripts, which was especially evident in  
330 the pile-up of ribosomal footprints in the 5' segment of the *gvpA* transcript. This putative post-  
331 transcriptional repression of translation resulted in growth-associated dilution of Gvp protein  
332 abundance, despite a steady increase at the mRNA level (Figure 7AC; Figure S10). As a  
333 consequence, GvpD protein abundance dropped below the abovementioned threshold, disrupting  
334 its ability to drive continued degradation of GvpE. This is consistent with the observation that  
335 GvpE protein was only detected in later stages of growth after GvpD abundance had decreased  
336 (Figure 7AC). Moreover, the appearance and subsequent increase in abundance of GvpE post-  
337 mid-exponential growth phase likely resulted in transcriptional activation of all *gvp* genes (Figure  
338 7AC). Indeed, mRNA levels of all *gvp* genes increased by >4-fold in mid-exponential growth phase  
339 (despite active cell division), unlike the moderate ( $\approx$ 2-fold) albeit steady increase observed in early  
340 and late phases of growth (Figure 7A). The transcriptional activation of all *gvp* genes likely  
341 overcame SmAP1, RNase\_2099C, and asRNA-mediated post-transcriptional repression to  
342 upregulate translation via increased ribosomal read through (Figure 7C; Figure S10). The  
343 resulting dramatic increase in abundance of proteins GvpN and GvpO, as well as the chaperone  
344 GvpF, potentially triggered the recruitment of GvpA to initiate gas vesicle assembly (66).  
345 Concomitantly, in the stationary phase, GvpD protein level increased above the threshold, likely  
346 restoring GvpE degradation, thereby disrupting transcriptional activation of *gvp* genes, and  
347 potentially terminating further translation of gas vesicle proteins (Figure 7C). So, in essence, the  
348 interplay between GvpD-mediated degradation of GvpE, transcriptional activation of *gvp* genes

349 by GvpE, and post-transcriptional repression of translation of *gvp* genes (likely mediated by  
350 SmAP1, asRNAs, and RNase\_2099C), together modulated timing of gas vesicle biogenesis. In  
351 this scheme, subtle changes in interplay across the different levels of regulation could drive rapid  
352 initiation or termination of gas vesicle biogenesis, given that the transcripts and the monomeric  
353 structural proteins are maintained at relatively high abundance, but the regulatory (GvpD and E)  
354 and some accessory proteins (e.g., GvpJ and L) are at significantly lower abundance across all  
355 growth phases.

356 **DISCUSSION**

357 This study has uncovered that a strikingly large proportion of protein-coding genes (54%) in the  
358 *H. salinarum* NRC-1 genome are potentially post-transcriptionally regulated. Notably, this  
359 estimate of the scale of post-transcriptional regulation is based on compilation of evidence from  
360 a limited set of contexts (i.e., primarily standard growth conditions). It is noteworthy that  
361 comparison of absolute and relative abundance changes in mRNA and protein levels just over  
362 batch culture growth has provided evidence for post-transcriptional control of 7% of all protein-  
363 coding genes. Different sets of genes were previously reported to have discordant relationship  
364 between mRNA and protein levels in other environmental contexts such as shifts in oxygen  
365 tension (44) and exposure to gamma irradiation (45). In response to gamma irradiation, 47  
366 upregulated transcripts had direction of change incompatible with their respective proteins. Of  
367 those, only five are included in the set of 188 putative post-transcriptionally regulated genes  
368 identified by the present study. Together, these observations illustrate the importance of  
369 environmental context in characterizing genome-wide implications of post-transcriptional  
370 regulation. Similarly, we have surveyed just three mechanisms (SmAP1, asRNAs, and one  
371 RNase) that provide likely mechanistic explanation for post-transcriptional regulation of 430 out  
372 of 966 transcripts (45%) with TPS. This suggests that the remaining TPS-associated 536  
373 transcripts are potentially post-transcriptionally regulated by other mechanisms, including  
374 endoribonucleases, trans-acting antisense RNAs and small regulatory RNAs (sRNAs) that were  
375 not surveyed in this study. Although, prior work has suggested a limited role for trans-acting  
376 antisense RNAs and sRNAs in archaeal regulation (71). Nonetheless, we can expect many more  
377 genes in the *H. salinarum* NRC-1 genome to be subject to post-transcriptional regulation,  
378 especially in ecological contexts that require rapid physiological state transitions for environmental  
379 acclimation.

380 Transcriptome-wide binding analysis with RIP-Seq implicated a global role for SmAP1 in  
381 post-transcriptional regulation of at least 397 genes. Action of SmAP1 in *H. salinarum* NRC-1  
382 appears to have mechanistic similarity to its counterparts in other archaea and also to Hfq in  
383 bacteria, such as preferentially targeting AU-rich sequences, and regulating itself (35).  
384 Autoregulation by the bacterial ortholog of SmAP1, Hfq, has also been reported previously in *E.*  
385 *coli* (72, 73) and *Sinorhizobium meliloti* (74). By reviewing RIP-Seq results from studies in other  
386 archaea we discovered that SmAP1 also binds to its own transcript in *S. solfataricus* (SSO6454)  
387 (33). The absence of evidence for autoregulation of SmAP1 in *H. volcanii* (31) is likely a technical  
388 artefact because the microarray used for RIP-ChIP interrogated binding to only non-coding RNAs,

389 and did not include probes for coding genes, including the SmAP1 CDS (HVO\_2723). Further,  
390 the genes targeted by SmAP1 also bear functional similarity with other organisms wherein SmAP1  
391 has been implicated in the regulation of motility (32, 75) and its ortholog has been implicated in  
392 regulation of transposition (59, 60). Notably, of the 32 non-redundant IS element-encoded  
393 proteins (Table S3) with above-average mRNA levels, only four were detected by SWATH-MS in  
394 this study, suggesting they were all post-transcriptionally repressed. By analyzing proteomics data  
395 from PeptideAtlas (76, 77) and PRIDE (78), including PXD003667 (79) and PXD015192 (80), we  
396 confirmed that 50% of the 32 transposases have been previously detected, depending on  
397 techniques and biological conditions. In addition, except for VNG\_0051a, we established that  
398 these proteins bear the features required for detection by SWATH-MS. With that reasoning, we  
399 posit that the lack of detection of transposases in this study is due to their low abundance or  
400 complete absence. Together these findings make a compelling case that translation of IS  
401 element-encoded transposases, and therefore transposition of mobile genetic elements, is post-  
402 transcriptionally regulated. Translational inhibition of transposases might have evolved as a fail-  
403 safe measure to prevent transposition in most contexts and allow their rapid activation in stressful  
404 environmental contexts, wherein benefits of genome reorganization could outweigh their  
405 deleterious effects (81).

406 Notwithstanding their mechanistic and functional similarities with counterparts in other  
407 archaea and even bacteria, we discovered that consequences of SmAP1-mediated regulation of  
408 transposition by some families of IS elements in *H. salinarum* NRC-1 are counterintuitive.  
409 Specifically, while we had expected that SmAP1 may likely repress translation of transposase  
410 transcripts, to our surprise we discovered that deletion of SmAP1 resulted in decreased frequency  
411 of transposition by IS elements of the IS4 and ISH3 families, which brought to fore two outstanding  
412 questions. First, in addition to directing targeted post-transcriptional processing and repression of  
413 transcripts, (how) does SmAP1 also mediate transposition by IS elements? And second, despite  
414 targeting AU-rich sequences how do SmAP1 and its counterparts accomplish regulation of  
415 specific subsets of target genes in a context-specific manner? While the first question will need  
416 further investigations into the mechanisms of SmAP1 action on transposition events, our  
417 integrated analysis has provided some clues to address the second question, such as evidence  
418 that SmAP1 might act in concert with other post-transcriptional regulatory mechanisms, viz.,  
419 asRNAs and RNase\_2099C to gain specificity for transcripts. So while SmAP1 appears to be  
420 expressed constitutively and maintained at median abundance (Figure S2B), its mode and target  
421 of action may be governed by other factors, such as conditional expression of asRNAs, which  
422 could possibly guide SmAP1 action on specific transcripts in a similar manner to its bacterial

423 counterpart (24). Indeed, in *H. volcanii* the global oxidative stress response upregulates asRNAs  
424 with consequential downregulation of specific transposase mRNAs, especially of the IS4 family  
425 (71). For example, SmAP1 and an asRNA may jointly regulate transposition events by binding to  
426 the 5' end of TnpB (VNG\_0042G) transcript to repress translation of this putative RNA-guided  
427 endonuclease, which is encoded by ISH39 (IS200/IS605 family) and possibly part of the  
428 transposition apparatus (Figure S11) (82, 83). Thus, SmAP1-mediated post-transcriptional  
429 regulation of mobile elements appears to have pleiotropic consequences depending on the IS  
430 family, with a repressive role for IS200/IS605, as reported previously for *S. enterica* (60), and an  
431 enhancer role for ISH3 and IS4. Indeed, SmAP1 might facilitate translation of transcripts,  
432 considering its hairpin-melting potential (84) and its role as a recruiter for translational complex  
433 subunits (85).

434 The current study has revealed extensive interplay of post-transcriptional regulation with  
435 regulation at other levels of information processing, which may mediate rapid adaptive responses  
436 to environmental change (e.g., genome reorganization by triggering transposition of IS elements,  
437 and vertical relocation by activating gas vesicle biogenesis). In the case of gas vesicle biogenesis,  
438 we observed that the high abundance and relative increase in transcript levels of the gas vesicle  
439 structural genes did not manifest in increased protein levels until the post-transcriptional  
440 repression of translation was overcome in later stages of growth, which is associated with  
441 stressful conditions including anoxia and nutrient limitation. Previously, we had demonstrated that  
442 RNase\_2099C is transcriptionally co-regulated with genes of the aerobic physiologic state but  
443 acts on transcripts of the anaerobic state (21). In this arrangement, the interplay of RNase\_2099C  
444 with transcriptional regulation generates an efficient state transition switch. For instance,  
445 RNase\_2099C-mediated repression of positive transcriptional autoregulation (RPAR) enables  
446 rapid shutdown of ATP-consuming K<sup>+</sup> uptake to conserve energy under anoxic conditions with  
447 high potassium availability. Gas vesicle biogenesis (response to light and oxygen) appears to be  
448 regulated in a similar set up albeit with an expanded set of players. Specifically, the interplay of  
449 GvpD-mediated degradation of GvpE, GvpE-mediated transcriptional activation of *gvp* genes, and  
450 post-transcriptional repression of gas vesicle protein synthesis through potential interplay of  
451 SmAP1, RNase\_2099C, and asRNAs is likely critical for mediating rapid initiation and termination  
452 of gas vesicle biogenesis. The genome-wide atlas reveals that a large proportion of genes in the  
453 *H. salinarum* NRC-1 genome is likely subject to such post-transcriptional regulation, and as such  
454 it will serve as an interactive hypothesis generator to drive in-depth characterization of specific  
455 mechanisms of rapid environmental acclimation.

456 **MATERIALS AND METHODS**

457 *Strains, media, and growth conditions*

458 We grew *Halobacterium salinarum* NRC-1 in complex media (CM; 250 g/L NaCl, 20 g/L  
459 MgSO<sub>4</sub>•7H<sub>2</sub>O, 3 g/L sodium citrate, 2 g/L KCl, and 10 g/L bacteriological peptone). Mutant strains,  
460 *Δura3* and *Δura3Δsmap1*, had their media supplemented with uracil (50 µg/mL). Vector harboring  
461 strains, wtp-pMTF-cMyc and wtp-pMTF-SmAP1-cMyc, had their media supplemented with  
462 mevinolin (20 µg/mL). All the cultures were grown at 37 °C, under light, and with constant agitation  
463 of 125 RPM (otherwise specified). For cloning steps, we used *Escherichia coli* DH5α grown in  
464 lysogeny broth (LB; 10 g/L tryptone, 5 g/L yeast extract, 10 g/L NaCl, pH 7.5) at 37 °C and under  
465 constant agitation. Carbenicillin (50 µg/mL) was added to LB when necessary.

466

467 *Construction of SmAP1 knockout strain and SmAP1 tagged strain*

468 SmAP1 knockout strain (*Δura3Δsmap1*; *ΔVNG\_1673GΔVNG\_1496G*) was constructed from a  
469 parent *Δura3* strain (*ΔVNG\_1673G*) by using the pop-in/pop-out method with two-step selection  
470 by mevinolin and 5-fluoroorotic acid (5-FOA) (86). Polymerase chain reaction (PCR) was used to  
471 confirm the genotype of null mutants selected by 5-FOA (Table S5). We evaluated the growth  
472 curve phenotype (Figure S12) by culturing strains in CM supplemented with uracil (50 µg/ml) at  
473 37 °C and 125 RPM.

474 To create the recombinant protein SmAP1-cMyc, we used the pMTF-cMyc vector (4).  
475 The SmAP1 encoding gene (VNG\_1496G) was amplified (Table S5) and purified using QIAquick  
476 PCR Purification (QIAGEN). The amplification product was cloned into the vector pMTF-cMyc,  
477 upstream to the region encoding 13-cMyc tag. The procedure was carried out by digesting pMTF-  
478 cMyc with endonucleases NdeI and BamHI (Fermentas) with further ligation of *smap1* amplicon  
479 by T4 DNA ligase (Fermentas). The clone was transformed into *E. coli* DH5α and confirmed by  
480 PCR and Sanger sequencing. Vectors were extracted and transformed into *H. salinarum* NRC-1  
481 strain to create strains wtp-pMTF-SmAP1-cMyc (SmAP1-cMyc overexpression) and wtp-pMTF-  
482 cMyc (cMyc-overexpression).

483

484

485 *SmAP1-RNA co-immunoprecipitation*

486 *H. salinarum* strains wtp-pMTF-SmAP1-cMyc and wtp-pMTF-cMyc were grown until they reached  
487 OD<sub>600nm</sub> ≈ 0.75. We centrifuged 20 mL of cell culture at 3,700 RCF for 10 minutes and  
488 resuspended cells in 12 mL of basal solution (CM without bacteriological peptone). The cellular  
489 suspension solution was transferred to Petri dishes, on ice, and submitted to 800x100 μJ/cm<sup>2</sup>  
490 ultraviolet (UV) radiation inside a UVC 500 Crosslinker (Amersham Biosciences). It was carefully  
491 transferred to 50 mL tubes and centrifuged at 3,700 RCF for 15 minutes at 4 °C. Cells were  
492 resuspended in 1 mL of lysis solution (1x PBS, 0.1% SDS, 0.5% deoxycholate, 0.5% NP-40,  
493 proteinase inhibitor—1 tablet for 100 mL (Sigma S8830), RNaseOUT inhibitor—2 μL/10 mL  
494 (Invitrogen)) and ice incubated for five minutes. The suspension was centrifuged at 10,000 RCF  
495 for five minutes at 4 °C. The supernatant was separated and incubated with 10 μL of Dynabeads  
496 M-450 anti-mouse IgG (Invitrogen #11041) for 10 minutes, at 4 °C, to remove spurious  
497 interactions. After incubation, the solution was centrifuged at 10,000 RCF for five minutes at 4 °C.  
498 The supernatant was incubated overnight, under constant agitation, at 4 °C, with 60 μL of anti-  
499 cMyc (antibody) coated beads (Sigma M4439). Beads were immobilized using a magnetic rack  
500 and washed twice using 1 mL of lysis solution, followed by two rounds of washing with 1 mL of  
501 saline solution (5x PBS, 0.1% SDS, 0.5% deoxycholate, 0.5% NP-40), and finally washed with 1  
502 mL of Tris-EDTA (TE buffer). Beads were resuspended in 100 μL of TE and incubated at 65 °C  
503 for 10 minutes. The suspension was centrifuged at 14,000 RCF for 30 minutes at 25 °C. We  
504 added 120 μL of TE/SDS (SDS 0.1%) to the supernatant and incubated it for 30 minutes at 65  
505 °C. Two aliquots were separated: i) one destined to the western blot assay; and ii) another  
506 destined to the RNA isolation prior to sequencing.

507

508 *SmAP1-cMyc western blot assay*

509 We verified the presence of the SmAP1 protein in the co-immunoprecipitated samples using the  
510 western blot assay. Aliquots were added of sample buffer (30% glycerol (v/v), 9.2% SDS (w/v),  
511 1% bromophenol blue (w/v), 20% β-mercaptoethanol (v/v), 0.25 M Tris-HCl pH 7.0) and denatured  
512 at 95 °C for five minutes. Denatured samples (20 μL) were submitted to 10% polyacrylamide gel  
513 electrophoresis (SDS-PAGE). PageRuler Prestained Protein Ladder (Fermentas) was used as  
514 weight marker and transference control. Gel and Hybond ECL nitrocellulose membrane (GE) were  
515 dipped in transfer buffer for 10 minutes.

516                   The membrane transfer was performed at 100 V for one hour. The membrane was  
517                   washed with PBS-T (0.1% Tween 20 (v/v)) and incubated in PBS-T with milk at room temperature  
518                   for one hour. After the blocking step, the membrane was quickly washed twice with PBS-T. The  
519                   primary antibody (anti-cMyc) was diluted (1:3,000) in PBS-T, and incubation was carried out at 4  
520                   °C, under constant agitation, overnight. The membrane was rewashed with PBS-T and incubated  
521                   in PBS-T at room temperature, under constant agitation for 15 minutes. The secondary antibody  
522                   (anti-mouse IgG-peroxidase - Sigma A4416) was diluted (1:3,000) in PBS-T, and incubation was  
523                   carried out at room temperature, under constant agitation, for one hour. The membrane was  
524                   quickly washed twice using PBS-T and incubated in PBS-T at room temperature, under constant  
525                   agitation, for 15 minutes. We used the reagents ECL Western Blotting Detection (GE) to develop  
526                   the membrane, and images were obtained using ChemiDoc XRS+ (Bio-Rad).

527

#### 528 *SmAP1 RIP-Seq and data analysis*

529                   The co-immunoprecipitated RNA samples were submitted to protein digestion using proteinase K  
530                   (Fermentas) and purified using the MinElute Reaction Cleanup Kit (QIAGEN) with a DNase  
531                   treatment step. We quantified the RNA samples using Quant-iT RiboGreen RNA Assay  
532                   (Invitrogen) and prepared them for sequencing using the TruSeq mRNA Stranded kit (Illumina).  
533                   Before sequencing, to equalize the concentrations, quantification was performed by using the  
534                   KAPA Library Quant kit (Kapa Biosystems). Samples were sequenced using the MiSeq Reagent  
535                   v2 kit (Illumina) for 50 cycles, using the single-end mode, in a MiSeq instrument (Illumina).

536                   We processed the sequenced libraries using the ripper pipeline (Table S6) to obtain  
537                   putative SmAP1 binding regions. Briefly, the software: i) trims the bad quality ends and adapters  
538                   from reads using Trimmomatic (87); ii) aligns trimmed reads to the reference genome (NCBI  
539                   Assembly ASM680v1) using HISAT2 (88) without gaps, splicing, or soft-clipping; iii) converts  
540                   alignment files from SAM to BAM format using SAMtools (89); iv) adjusts multi-mapping reads  
541                   using MMR (90); v) computes single-nucleotide resolution transcriptome signal using BEDtools  
542                   (91); vi) computes a coordinate-wise  $\log_2$  fold change between co-immunoprecipitated samples  
543                   relative to control samples and identify regions with at least ten consecutive nucleotides satisfying  
544                    $\log_2$  fold change  $\geq 1$ . Interaction regions for two biological replicates (BR1 and BR2) were merged,  
545                   since their intersection of SmAP1-bound genes had a 3.8-fold enrichment over the expected value  
546                   (observed: 157; expected: 41.44;  $p$ -value =  $3.14 \times 10^{-71}$ ). We tested the fold enrichment  
547                   significance by using the SuperExactTest::MSET function (92).

548 *Preparation and acquisition of proteomics samples*

549 Sample preparation and data acquisition for the time-course measurements of the *H. salinarum*  
550 proteome were performed as described in Kusebauch et al. (in preparation). *H. salinarum* NRC-  
551 1 was cultured in CM. Cultures were grown in triplicate (37°C, shaking at 220 RPM) and  
552 illuminated ( $\approx$ 20  $\mu$ mol/m<sup>2</sup>/sec) in Innova 9400 incubators (New Brunswick). Cultures were  
553 harvested at four time points: early exponential phase ( $OD_{600nm} = 0.2$ ; 14.3 hours), mid-  
554 exponential phase ( $OD_{600nm} = 0.5$ ; 21.5 hours), late exponential phase ( $OD_{600nm} = 0.8$ ; 28.8 hours),  
555 and stationary phase (40.8 hours). Cells were collected by centrifugation (8,000 x g, 2 minutes,  
556 4°C). Cell pellets were resuspended in Milli-Q water and disrupted at 4°C using ceramic beads  
557 (Mo Bio Laboratories) and a Precellys 24 homogenizer (Bertin Corp). Protein content was  
558 determined by bicinchoninic acid assay (BCA) (Thermo-Fisher). Proteins were reduced (5mM  
559 Dithiothreitol (DDT, 45 minutes, 37 °C)), alkylated (14 mM iodoacetamide (30 minutes, room  
560 temperature, darkness)), and digested with trypsin (1:50 enzyme:substrate ratio, 37°C, 16 h).  
561 Samples were desalted with tC18 SepPak cartridges (Waters). Sample analysis was performed  
562 on a TripleTOF® 5600+ system equipped with a Nanospray-III® Source (Sciex) and an Eksigent  
563 Ekspert™ nanoLC 425 with cHiPLC® system in trap-elute mode (Sciex). Peptides were separated  
564 with a gradient from 3% to 33% of 0.1% formic acid in acetonitrile (v/v) for 120 minutes. Data were  
565 collected in MS/MS<sup>ALL</sup> SWATH™ acquisition mode using 100 variable acquisition windows.

566

567 *SWATH-MS data analysis*

568 SWATH-MS data were analyzed with the Spectronaut software (version 15.5.211111.50606) and  
569 an assay library for *H. salinarum* NRC-1 reported in Kusebauch et al. (in preparation). SWATH  
570 .wiff raw data files were converted to HTRMS files with the Spectronaut HTRMS converter  
571 (15.5.211111.50606). Data extraction mass tolerance (MS1 and MS2) was set to dynamic with a  
572 correction factor of 1. Dynamic extracted ion chromatogram (XIC) RT window was enabled with  
573 a correction factor of 1 and local (non-linear) RT regression. Decoy assays were dynamically  
574 generated using the scrambled decoy method and library size fraction set to 1. The identification  
575 was performed using the normal distribution estimator with precursor identification results with *q*-  
576 value (false discovery rate; FDR) < 0.1 and protein identification results with a *q*-value (FDR) <  
577 0.01. Quantification was performed with interference correction enabled, MS2 ion peak areas of  
578 quantified peptides were summed to estimate protein peak areas, and area as quantity type  
579 selected. Identified precursor quantities were normalized using the Spectronaut built-in global  
580 normalization function (median). The four time points in this study were defined as four conditions

581 in the condition setup. We used Spectronaut's protein quantification and proDA (93) to perform  
582 differential expression analysis of proteins. We computed the contrasts of interest and set up  $|\log_2$   
583 fold change|  $\geq 1$  and adjusted  $p$ -value  $< 0.05$  as the criteria to determine differentially expressed  
584 proteins.

585

586 *Non-redundant reference transcriptome*

587 Many annotation efforts for *H. salinarum* NRC-1 have been made available since the publication  
588 of its genome assembly (49). Consequently, cross-referencing findings from publications using  
589 different sources has become a challenging and time-consuming task. Moreover, the genome  
590 presents redundancy in terms of (quasi)identical paralogs, most of them found within plasmid  
591 repetitive regions (94) and contained within multi-copy insertion sequences (95). To solve the  
592 problem of the annotation multiplicity and gene redundancy, we extracted coding and non-coding  
593 sequences (tRNAs, rRNAs, Signal Recognition Particle RNA, and RNase P) from different  
594 annotation sources for *H. salinarum* NRC-1 and R1 strains (Table S1) and clustered them using  
595 CD-HIT (96). Coding and non-coding genes with at least 95% and 99% global amino acid and  
596 nucleotide identity, respectively, were grouped and represented by a single entity anchored by  
597 the sequence and locus tag given by the latest large-scale annotation effort for *H. salinarum* NRC-  
598 1 (50). We only considered sequences represented in this annotation. We also collected and  
599 parsed clusters of orthologous genes (COG) (97) to functionally categorize the non-redundant  
600 reference transcriptome, and classified insertion sequence families using ISfinder (56) and ISSaga  
601 (98) platforms. The code to reproduce this annotation simplification effort is available on GitHub  
602 (see halo\_nr\_tx in Table S6).

603

604 *Transcriptome analysis*

605 We retrieved RNA-Seq and Ribo-Seq data from a *H. salinarum*'s growth curve experiment  
606 available at NCBI SRA under accession PRJNA413990 (42). The samples are the same for which  
607 the proteome data was generated, as explained previously. We quantified all the RNA-Seq  
608 libraries by mapping them against the *H. salinarum* NRC-1 non-redundant reference  
609 transcriptome using kallisto (99) facilitated by the use of the pipeline runKallisto (Table S6). We  
610 performed differential expression analysis for the RNA-Seq and Ribo-Seq time course experiment  
611 (42) using DESeq2 (100). Only genes satisfying  $|\log_2$  fold change|  $\geq 1$  and adjusted  $p$ -value  $<$   
612 0.05 were considered differentially expressed. We generated the transcriptome coverage signal  
613 for genome browsing using the frtc pipeline (101) (Table S6). Briefly, the tool trims reads using

614 Trimmomatic (87); aligns them to the reference genome (NCBI Assembly ASM680v1) using  
615 HISAT2 without splicing (88); adjusts multi-mapping instances using MMR (90); and computes  
616 the genome-wide coverage using deepTools2 (102).

617 We performed differential expression analysis of strain  $\Delta RNase\_2099C$  by reanalyzing  
618 data from (21), deposited in Gene Expression Omnibus (GEO) under accession GSE45988.  
619 Briefly, we used limma (103) to process the data and computed the  $\Delta RNase\_2099C$  vs.  $\Delta ura3$   
620 contrast controlling for the growth curve time point effect. We only used mid-exponential ( $OD_{600nm}$   
621  $\approx 0.4$ ) and late-exponential ( $OD_{600nm} \approx 0.8$ ) growth phase data. Only genes satisfying  $|\log_2$  fold  
622 change|  $\geq 1$  and  $p$ -value  $< 0.05$  were considered differentially expressed.

623

624 *Inference of putative post-transcriptionally regulated genes*

625 We relied on transcriptome and proteome quantitation to infer putative post-transcriptionally  
626 regulated genes. For that, we developed two methods: i) the absolute abundance-based  
627 approach, in which we identified genes producing simultaneously high mRNA levels (transcripts  
628 per million, TPM, in the upper quintile) and low protein abundance (lower quintile or undetected);  
629 and ii) the relative abundance-based approach, in which we inspected differentially expressed  
630 genes in physiological state transitions having mRNA levels being upregulated whilst protein  
631 levels being downregulated.

632 We further inspected genes identified by the absolute abundance-based approach,  
633 whose proteins were not detected, to remove entries likely missed due to technical limitations.  
634 After manual inspection, we removed potential transmembrane proteins (as these are difficult to  
635 be detected), proteins not represented in the assay library due to the lack of suitable peptides for  
636 detection by SWATH-MS (e.g., hydrophobicity, peptide length), and proteins not represented in  
637 the assay library due to differences in annotation versions. To be considered a transmembrane  
638 protein, we first conducted a transmembrane domain prediction for all the entries encoded by the  
639 non-redundant transcriptome using TOPCONS webserver (104). We manually inspected the  
640 results and evaluated the “consensus prediction probability” of transmembrane regions. We  
641 required proteins to have at least one transmembrane domain with a considerable extension  
642 satisfying probability  $\geq 0.9$ . To aid our judgement, we also pondered empirical evidence (105,  
643 106) and functional annotation. This approach identified 117 genes with expressive mRNA and  
644 undetected proteins with a high likelihood of being post-transcriptionally regulated (File S3).

645

646 *Long-read DNA sequencing and analysis*

647 *H. salinarum* strains  $\Delta$ ura3 and  $\Delta$ ura3 $\Delta$ smap1 were grown in CM supplemented with uracil until  
648 OD<sub>600nm</sub>  $\approx$  0.5. Aliquots of 2 mL of cell cultures were submitted to DNA extraction using DNeasy  
649 Blood & Tissue kit (QIAGEN). DNA samples were quality checked and genotyped using PCR to  
650 confirm strains (Table S5). We prepared the samples for long-read DNA sequencing using the  
651 MinION platform (Oxford Nanopore Technologies, ONT). Libraries were prepared using SQK-  
652 LSK108 (ONT) combined with EXP-NBD103 (ONT) to allow multiplexing. The experiment was  
653 run using MinION Mk1B (ONT) in a FLO-MIN106 (ONT) flow cell for 48 hours. Raw data were  
654 demultiplexed using Deepbinner (107), and base called by Guppy (ONT). Quality checking was  
655 done using Filtlong (Table S6), and adapter trimming was performed using Porechop (Table S6).

656 We used NGMLR (108) to align reads to a modified version of reference genome, which  
657 excludes long duplications (NC\_002607.1:1-2,014,239, NC\_001869.1:1-150,252,  
658 NC\_002608.1:112,796-332,792). To identify structural variations (SV), the alignments were  
659 processed with Sniffles (108), and the VCF files were filtered to keep only insertions and deletions.  
660 The sequences of detected SVs were compared to *H. salinarum* NRC-1 annotated insertion  
661 sequences using BLAST (109). Insertions and excisions were only annotated if satisfying the  
662 threshold of at least 75% identity, 80% coverage considering both query and subject. These  
663 criteria were based on the 80-80-80 rule proposed by (110), but slightly loosened because of  
664 Nanopore intrinsic high error rates.

665 We applied a clustering approach for neighbor elements to avoid overestimating the  
666 number of identified SVs. SVs of the same class (insertion or excision), caused by the same  
667 element, and starting within 50 base pairs of distance from each other, were combined into a  
668 single cluster having a mean start point and a support index based on the number of occurrences.  
669 Dividing this number of occurrences (e) by the local read coverage (25-nucleotide bidirectional  
670 flank) (c) allowed us to classify SV clusters in three categories: i) When  $e/c \leq 0.1$ , the cluster is  
671 defined as relatively rare in the population; ii) When  $0.1 < e/c \leq 0.5$ , it is common; iii) When  $e/c >$   
672 0.5, it is characterized as predominant, indicating this SV might be fixed in the population  
673 genomes.

674 We computed the total number of clusters of insertions and excisions for each of the  
675 libraries and added them up before normalizing the values based on each sample's total of aligned  
676 reads. To normalize, we identified the library with the biggest number of aligned reads and  
677 adjusted the others to be comparable. The mean value for normalized counts was computed for

678 both  $\Deltaura3\Deltasmap1$  and  $\Deltaura3$  and compared using a confidence interval of 68% (see Table S6  
679 for code).

680

681 *Enrichment analysis and average comparison*

682 To detect enriched features (e.g., SmAP1 binding, asRNA, and TPS) within groups of genes, we  
683 performed enrichment analysis using the hypergeometric test from R software (stats::phyper  
684 function). To compare the average of features (e.g., half-lives, CAI, GC, and  $\Delta RNase\_2099C \log_2$   
685 fold change (LFC)) between groups of genes, we used the nonparametric Mann–Whitney U test  
686 from R software (stats::wilcox.test function). The significance cutoff of our choice for both  
687 statistical tests was  $p$ -value  $< 0.05$ .

688

689 *Data collection from miscellaneous sources*

690 We gathered and parsed data from several sources. We collected antisense RNA (asRNA) data  
691 from Table S4 of (46). We obtained transcript processing sites (TPS) from Table S1 of (47).  
692 Redundancy was removed by collapsing asRNAs and TPS of identical and (quasi)identical  
693 transcripts. We obtained half-lives from a microarray experiment (43). The redundancy was  
694 removed by computing the average half-lives of identical and (quasi)identical genes. We  
695 computed the codon adaptation index (CAI) (111) using the coRdon::CAI function (see coRdon  
696 in Table S6), taking as input the 5% most abundant proteins according to our proteomics  
697 approach. We computed the GC content (guanine-cytosine content) using the  
698 Biostrings::letterFrequency function.

699

700 *H. salinarum NRC-1 multi-omics Atlas portal*

701 We developed the *H. salinarum* NRC-1 multi-omics Atlas portal by integrating existing  
702 components to new resources. Legacy data is stored in an SBEAMS MS SQL Server database  
703 which supplements the main MySQL database. A web service API implemented in Python and  
704 Flask provides uniform access to these resources. We implemented the web-based user interface  
705 using the Javascript framework Vue.js (see Table S6 for code). We built the heatmap interface  
706 with the help of InteractiveComplexHeatmap (112), ComplexHeatmap (113), and Shiny R  
707 packages. We built the genome browser by using igv.js (114). Data used to generate heatmaps  
708 were prepared as described in previous sections with an additional step for scale adjustment

709 allowing a graphical representation of disparate multimodal omics sources. The quantile  
710 normalized data is also available along with the non-normalized data (File S1). The web portal is  
711 available at <http://halodata.systemsbiology.net>.

712

713 *Data and code availability*

714 SmAP1 RIP-Seq raw data (FASTQ format) and DNA-Seq data (demultiplexed, base called, and  
715 trimmed; FASTQ format) were deposited in NCBI's Sequence Read Archive and are publicly  
716 available under the BioProject accession PRJNA808788. Raw DNA-Seq data (FAST5 format) is  
717 available at Zenodo under the digital object identifier 10.5281/zenodo.6303948 (accession  
718 6303948). The code used in this study is available on GitHub in multiple repositories (see Table  
719 S6 for links and description).

720

## 721 **CREDIT AUTHORSHIP CONTRIBUTION STATEMENT**

722 APRL: Methodology, Software, Validation, Formal analysis, Investigation, Data Curation, Writing  
723 — Original Draft, Writing — Review & Editing, Visualization; UK: Methodology, Investigation,  
724 Formal analysis, Writing — Review & Editing; LSZ: Methodology, Investigation; WJW: Software,  
725 Data Curation, Visualization; JPPA: Methodology, Validation, Formal analysis, Investigation, Data  
726 Curation, Writing — Review & Editing; ST: Software, Data Curation, Writing — Review & Editing,  
727 Visualization; ALGL: Conceptualization, Writing — Review & Editing, Supervision; JVGF:  
728 Conceptualization, Writing — Review & Editing, Methodology, Investigation; RZNV:  
729 Conceptualization, Validation, Writing — Review & Editing, Supervision; RLM: Conceptualization,  
730 Resources, Writing — Review & Editing, Supervision, Project administration, Funding acquisition;  
731 TK: Conceptualization, Resources, Supervision, Project administration, Funding acquisition;  
732 NSB: Conceptualization, Resources, Writing — Original Draft, Writing — Review & Editing,  
733 Visualization, Supervision, Project administration, Funding acquisition.

734

## 735 **DECLARATION OF CONFLICTING INTERESTS**

736 All authors declare that they do not have conflicts of interest.

737

738 **ACKNOWLEDGMENTS**

739 We thank Dr. Alessandro de Mello Varani for helping us with insertion sequence family annotation;  
740 Silvia Helena Epifânio and Min Pan for the laboratory technical support; Catarina dos Santos  
741 Gomes for helping in the execution of long-read DNA sequencing; Dr. Elisabeth Wurtmann for  
742 helping with the RIP-Seq assay standardization.

743

744 **FUNDING**

745 APRL was supported by a fellowship granted by the São Paulo Research Foundation (FAPESP;  
746 grants #2017/03052-2 and #2019/13440-5). LSZ and JVGF were supported by FAPESP  
747 fellowships #2011/07487-7 and #2013/21522-5, respectively. TK was supported by FAPESP  
748 grants #2009/09532-0 and #2015/21038-1. This study was partially funded by grants from the  
749 National Institutes of Health, National Institute of General Medical Sciences (R01GM087221 to  
750 RLM), the Office of the Director (S10OD026936 to RLM), and the National Science Foundation  
751 (awards DBI-1920268 to RLM, MCB-1616955 to NB and RLM, and MCB-2105570 to NB and ST).  
752 This study was also supported by the *Coordenação de Aperfeiçoamento de Pessoal de Nível*  
753 *Superior—Brasil* (CAPES)—Finance Code 001, and *Fundação de Apoio ao Ensino, Pesquisa e*  
754 *Assistência do Hospital das Clínicas da Faculdade de Medicina de Ribeirão Preto da*  
755 *Universidade de São Paulo* (FAEPA).

756 **REFERENCES**

- 757 1. Bauer MA, Kainz K, Carmona-Gutierrez D, Madeo F. 2018. Microbial wars: Competition  
758 in ecological niches and within the microbiome. *Microb Cell* 5:215–219.
- 759 2. Bonneau R, Facciotti MT, Reiss DJ, Schmid AK, Pan M, Kaur A, Thorsson V, Shannon P,  
760 Johnson MH, Bare JC, Longabaugh W, Vuthoori M, Whitehead K, Madar A, Suzuki L,  
761 Mori T, Chang D-E, Diruggiero J, Johnson CH, Hood L, Baliga NS. 2007. A predictive  
762 model for transcriptional control of physiology in a free living cell. *Cell* 131:1354–1365.
- 763 3. Brooks AN, Reiss DJ, Allard A, Wu W-J, Salvanha DM, Plaisier CL, Chandrasekaran S,  
764 Pan M, Kaur A, Baliga NS. 2014. A system-level model for the microbial regulatory  
765 genome. *Mol Syst Biol* 10:740.
- 766 4. Facciotti MT, Reiss DJ, Pan M, Kaur A, Vuthoori M, Bonneau R, Shannon P, Srivastava  
767 A, Donohoe SM, Hood LE, Baliga NS. 2007. General transcription factor specified global  
768 gene regulation in archaea. *Proc Natl Acad Sci U S A* 104:4630–4635.
- 769 5. Koide T, Reiss DJ, Bare JC, Pang WL, Facciotti MT, Schmid AK, Pan M, Marzolf B, Van  
770 PT, Lo F-Y, Pratap A, Deutsch EW, Peterson A, Martin D, Baliga NS. 2009. Prevalence of  
771 transcription promoters within archaeal operons and coding sequences. *Mol Syst Biol*  
772 5:285.
- 773 6. Facciotti MT, Pang WL, Lo F, Whitehead K, Koide T, Masumura K, Pan M, Kaur A,  
774 Larsen DJ, Reiss DJ, Hoang L, Kalisiak E, Northen T, Trauger SA, Siuzdak G, Baliga NS.  
775 2010. Large scale physiological readjustment during growth enables rapid,  
776 comprehensive and inexpensive systems analysis. *BMC Syst Biol* 4:64.
- 777 7. Martínez LC, Vadyvaloo V. 2014. Mechanisms of post-transcriptional gene regulation in  
778 bacterial biofilms. *Front Cell Infect Microbiol* 4:38.
- 779 8. Ashworth J, Wurtmann EJ, Baliga NS. 2012. Reverse engineering systems models of  
780 regulation: discovery, prediction and mechanisms. *Curr Opin Biotechnol* 23:598–603.
- 781 9. Brooks AN, Turkarslan S, Beer KD, Lo FY, Baliga NS. 2011. Adaptation of cells to new  
782 environments. *Wiley Interdiscip Rev Syst Biol Med* 3:544–561.
- 783 10. Koide T, Pang WL, Baliga NS. 2009. The role of predictive modelling in rationally re-  
784 engineering biological systems. *Nat Rev Microbiol* 7:297–305.
- 785 11. Otwell AE, López García de Lomana A, Gibbons SM, Orellana MV, Baliga NS. 2018.  
786 Systems biology approaches towards predictive microbial ecology. *Environ Microbiol*  
787 20:4197–4209.
- 788 12. Shu W-S, Huang L-N. 2022. Microbial diversity in extreme environments. *Nat Rev  
789 Microbiol* 20:219–235.
- 790 13. Allers T, Mevarech M. 2005. Archaeal genetics — the third way. *Nat Rev Genet* 6:58–73.
- 791 14. Bell SD, Jackson SP. 2001. Mechanism and regulation of transcription in archaea. *Curr  
792 Opin Microbiol* 4:208–213.
- 793 15. Martinez-Pastor M, Tonner PD, Darnell CL, Schmid AK. 2017. Transcriptional Regulation  
794 in Archaea: From Individual Genes to Global Regulatory Networks. *Annu Rev Genet*  
795 51:143–170.

796 16. Qi L, Yue L, Feng D, Qi F, Li J, Dong X. 2017. Genome-wide mRNA processing in  
797 methanogenic archaea reveals post-transcriptional regulation of ribosomal protein  
798 synthesis. *Nucleic Acids Res* 45:7285–7298.

799 17. Li J, Qi L, Guo Y, Yue L, Li Y, Ge W, Wu J, Shi W, Dong X. 2015. Global mapping  
800 transcriptional start sites revealed both transcriptional and post-transcriptional regulation  
801 of cold adaptation in the methanogenic archaeon *Methanolobus psychrophilus*. *Sci Rep*  
802 5:9209.

803 18. Jäger D, Pernitzsch SR, Richter AS, Backofen R, Sharma CM, Schmitz RA. 2012. An  
804 archaeal sRNA targeting cis- and trans-encoded mRNAs via two distinct domains.  
805 *Nucleic Acids Res* 40:10964–10979.

806 19. Prasse D, Förstner KU, Jäger D, Backofen R, Schmitz RA. 2017. sRNA<sub>154</sub> a newly  
807 identified regulator of nitrogen fixation in *Methanosarcina mazei* strain Gö1. *RNA Biol*  
808 14:1544–1558.

809 20. Jia J, Li J, Qi L, Li L, Yue L, Dong X. 2021. Post-transcriptional regulation is involved in  
810 the cold-active methanol-based methanogenic pathway of a psychrophilic methanogen.  
811 *Environ Microbiol* 23:3773–3788.

812 21. Wurtmann EJ, Ratushny AV, Pan M, Beer KD, Aitchison JD, Baliga NS. 2014. An  
813 evolutionarily conserved RNase-based mechanism for repression of transcriptional  
814 positive autoregulation. *Mol Microbiol* 92:369–382.

815 22. Van Assche E, Van Puyvelde S, Vanderleyden J, Steenackers HP. 2015. RNA-binding  
816 proteins involved in post-transcriptional regulation in bacteria. *Front Microbiol* 6:141.

817 23. Azam MS, Vanderpool CK. 2018. Translational regulation by bacterial small RNAs via an  
818 unusual Hfq-dependent mechanism. *Nucleic Acids Res* 46:2585–2599.

819 24. Vogel J, Luisi BF. 2011. Hfq and its constellation of RNA. *Nat Rev Microbiol* 9:578–589.

820 25. Chapman EJ, Carrington JC. 2007. Specialization and evolution of endogenous small  
821 RNA pathways. *Nat Rev Genet* 8:884–896.

822 26. Collins BM, Harrop SJ, Kornfeld GD, Dawes IW, Curmi PMG, Mabbott BC. 2001. Crystal  
823 structure of a heptameric Sm-like protein complex from archaea: implications for the  
824 structure and evolution of snRNPs. *J Mol Biol* 309:915–923.

825 27. Kilic T, Thore S, Suck D. 2005. Crystal structure of an archaeal Sm protein from  
826 *Sulfolobus solfataricus*. *Proteins* 61:689–693.

827 28. Thore S, Mayer C, Sauter C, Weeks S, Suck D. 2003. Crystal Structures of the  
828 *Pyrococcus abyssi* Sm Core and Its Complex with RNA: COMMON FEATURES OF RNA  
829 BINDING IN ARCHAEA AND EUKARYA. *J Biol Chem* 278:1239–1247.

830 29. Törö I, Basquin J, Teo-Dreher H, Suck D. 2002. Archaeal Sm Proteins form Heptameric  
831 and Hexameric Complexes: Crystal Structures of the Sm1 and Sm2 Proteins from the  
832 Hyperthermophile *Archaeoglobus fulgidus*. *J Mol Biol* 320:129–142.

833 30. Fando MS, Mikhaylina AO, Lekontseva NV, Tishchenko SV, Nikulin AD. 2021. Structure  
834 and RNA-Binding Properties of Lsm Protein from *Halobacterium salinarum*. *Biochemistry*  
835 (Mosc) 86:833–842.

836 31. Fischer S, Benz J, Späth B, Maier L-K, Straub J, Granzow M, Raabe M, Urlaub H,  
837 Hoffmann J, Brutschy B, Allers T, Soppa J, Marchfelder A. 2010. The archaeal Lsm  
838 protein binds to small RNAs. *J Biol Chem* 285:34429–34438.

839 32. Maier LK, Benz J, Fischer S, Alstetter M, Jaschinski K, Hilker R, Becker A, Allers T,  
840 Soppa J, Marchfelder A. 2015. Deletion of the Sm1 encoding motif in the *lsm* gene results  
841 in distinct changes in the transcriptome and enhanced swarming activity of *Haloferax*  
842 cells. *Biochimie* 117:129–137.

843 33. Märtens B, Bezerra GA, Kreuter MJ, Grishkovskaya I, Manica A, Arkhipova V, Djinovic-  
844 Carugo K, Bläsi U. 2015. The Heptameric SmAP1 and SmAP2 Proteins of the  
845 Crenarchaeon *Sulfolobus solfataricus* Bind to Common and Distinct RNA Targets. *Life*  
846 (Basel) 5:1264–1281.

847 34. Clouet-d'Orval B, Batista M, Bouvier M, Quentin Y, Fichant G, Marchfelder A, Maier L-K.  
848 2018. Insights into RNA-processing pathways and associated RNA-degrading enzymes in  
849 Archaea. *FEMS Microbiol Rev* 42:579–613.

850 35. Reichelt R, Grohmann D, Willkomm S. 2018. A journey through the evolutionary  
851 diversification of archaeal Lsm and Hfq proteins. *Emerg Top Life Sci* 2:647–657.

852 36. Gelsinger DR, DiRuggiero J. 2018. The Non-Coding Regulatory RNA Revolution in  
853 Archaea. *Genes* (Basel) 9.

854 37. Turkarslan S, Reiss DJ, Gibbins G, Su WL, Pan M, Bare JC, Plaisier CL, Baliga NS.  
855 2011. Niche adaptation by expansion and reprogramming of general transcription factors.  
856 *Mol Syst Biol* 7:554.

857 38. DasSarma S. 1989. Mechanisms of genetic variability in *Halobacterium halobium*: the  
858 purple membrane and gas vesicle mutations. *Can J Microbiol* 35:65–72.

859 39. Kunka KS, Griffith JM, Holdener C, Bischof KM, Li H, DasSarma P, DasSarma S,  
860 Slonczewski JL. 2020. Acid Experimental Evolution of the Haloarchaeon *Halobacterium*  
861 sp. NRC-1 Selects Mutations Affecting Arginine Transport and Catabolism. *Front*  
862 *Microbiol* 11.

863 40. Pfeifer F. 2015. Haloarchaea and the Formation of Gas Vesicles. *Life* (Basel) 5:385–402.

864 41. Grote M, O'Malley MA. 2011. Enlightening the life sciences: the history of halobacterial  
865 and microbial rhodopsin research. *FEMS Microbiol Rev* 35:1082–1099.

866 42. López García de Lomana A, Kusebauch U, Raman AV, Pan M, Turkarslan S, Lorenzetti  
867 APR, Moritz RL, Baliga NS. 2020. Selective Translation of Low Abundance and  
868 Upregulated Transcripts in *Halobacterium salinarum*. *mSystems* 5.

869 43. Hundt S, Zaigler A, Lange C, Soppa J, Klug G. 2007. Global analysis of mRNA decay in  
870 *Halobacterium salinarum* NRC-1 at single-gene resolution using DNA microarrays. *J*  
871 *Bacteriol* 189:6936–6944.

872 44. Schmid AK, Reiss DJ, Kaur A, Pan M, King N, Van PT, Hohmann L, Martin DB, Baliga  
873 NS. 2007. The anatomy of microbial cell state transitions in response to oxygen. *Genome*  
874 *Res* 17:1399–1413.

875 45. Whitehead K, Kish A, Pan M, Kaur A, Reiss DJ, King N, Hohmann L, DiRuggiero J,  
876 Baliga NS. 2006. An integrated systems approach for understanding cellular responses to  
877 gamma radiation. *Mol Syst Biol* 2:47.

878 46. de Almeida JPP, Vêncio RZN, Lorenzetti APR, Ten-Caten F, Gomes-Filho JV, Koide T.  
879 2019. The Primary Antisense Transcriptome of *Halobacterium salinarum* NRC-1. *Genes*  
880 (Basel) 10.

881 47. Ibrahim AGAE-R, Vêncio RZN, Lorenzetti APR, Koide T. 2021. *Halobacterium salinarum*  
882 and *Haloferax volcanii* Comparative Transcriptomics Reveals Conserved Transcriptional  
883 Processing Sites. *Genes (Basel)* 12:1018.

884 48. Li W, O'Neill KR, Haft DH, DiCuccio M, Chetvernin V, Badretdin A, Coulouris G, Chitsaz  
885 F, Derbyshire MK, Durkin AS, Gonzales NR, Gwadz M, Lanczycki CJ, Song JS, Thanki  
886 N, Wang J, Yamashita RA, Yang M, Zheng C, Marchler-Bauer A, Thibaud-Nissen F.  
887 2020. RefSeq: expanding the Prokaryotic Genome Annotation Pipeline reach with protein  
888 family model curation. *Nucleic Acids Res* 49:D1020–D1028.

889 49. Ng WV, Kennedy SP, Mahairas GG, Berquist B, Pan M, Shukla HD, Lasky SR, Baliga  
890 NS, Thorsson V, Sbrogna J, Swartzell S, Weir D, Hall J, Dahl TA, Welti R, Goo YA,  
891 Leithauser B, Keller K, Cruz R, Danson MJ, Hough DW, Maddocks DG, Jablonski PE,  
892 Krebs MP, Angevine CM, Dale H, Isenbarger TA, Peck RF, Pohlschroder M, Spudich JL,  
893 Jung K-H, Alam M, Freitas T, Hou S, Daniels CJ, Dennis PP, Omer AD, Ebhardt H, Lowe  
894 TM, Liang P, Riley M, Hood L, DasSarma S. 2000. Genome sequence of *Halobacterium*  
895 species NRC-1. *Proc Natl Acad Sci U S A* 97:12176–12181.

896 50. Pfeiffer F, Marchfelder A, Habermann B, Dyall-Smith ML. 2019. The Genome Sequence  
897 of the *Halobacterium salinarum* Type Strain Is Closely Related to That of Laboratory  
898 Strains NRC-1 and R1. *Microbiol Resour Announc* 8.

899 51. Achsel T, Stark H, Lührmann R. 2001. The Sm domain is an ancient RNA-binding motif  
900 with oligo(U) specificity. *Proc Natl Acad Sci U S A* 98:3685–3689.

901 52. Frumkin I, Lajoie MJ, Gregg CJ, Hornung G, Church GM, Pilpel Y. 2018. Codon usage of  
902 highly expressed genes affects proteome-wide translation efficiency. *Proc Natl Acad Sci*  
903 *U S A* 115.

904 53. Filee J, Siguier P, Chandler M. 2007. Insertion Sequence Diversity in Archaea. *Microbiol*  
905 *Mol Biol Rev* 71:121–157.

906 54. Siguier P, Gourbeyre E, Varani A, Ton-Hoang B, Chandler M. 2015. Everyman's Guide to  
907 Bacterial Insertion Sequences. *Microbiol Spectr* 3.

908 55. Kichenaradja P, Siguier P, Pérochon J, Chandler M. 2010. ISBrowser: an extension of  
909 ISfinder for visualizing insertion sequences in prokaryotic genomes. *Nucleic Acids Res*  
910 38:D62-68.

911 56. Siguier P, Pérochon J, Lestrade L, Mahillon J, Chandler M. 2006. ISfinder: the reference  
912 centre for bacterial insertion sequences. *Nucleic Acids Res* 34:D32–D36.

913 57. DasSarma S, RajBhandary UL, Khorana HG. 1983. High-frequency spontaneous  
914 mutation in the bacterio-opsin gene in *Halobacterium halobium* is mediated by  
915 transposable elements. *Proc Natl Acad Sci U S A* 80:2201–2205.

916 58. DasSarma S, Halladay JT, Jones JG, Donovan JW, Giannasca PJ, de Marsac NT. 1988.  
917 High-frequency mutations in a plasmid-encoded gas vesicle gene in *Halobacterium*  
918 *halobium*. Proc Natl Acad Sci U S A 85:6861–6865.

919 59. Ellis MJ, Trussler RS, Haniford DB. 2015. Hfq binds directly to the ribosome-binding site  
920 of IS10 transposase mRNA to inhibit translation. Mol Microbiol 96:633–650.

921 60. Ellis MJ, Trussler RS, Haniford DB. 2015. A cis-encoded sRNA, Hfq and mRNA  
922 secondary structure act independently to suppress IS200 transposition. Nucleic Acids  
923 Res 43:6511–6527.

924 61. Maillet N. 2020. Rapid Peptides Generator: fast and efficient in silico protein digestion.  
925 NAR Genom Bioinform 2.

926 62. Oren A. 2012. The function of gas vesicles in halophilic archaea and bacteria: theories  
927 and experimental evidence. Life (Basel) 3:1–20.

928 63. DasSarma S, Kennedy SP, Berquist B, Victor Ng W, Baliga NS, Spudich JL, Krebs MP,  
929 Eisen JA, Johnson CH, Hood L. 2001. Genomic perspective on the photobiology of  
930 *Halobacterium* species NRC-1, a phototrophic, phototactic, and UV-tolerant  
931 haloarchaeon. Photosynth Res 70:3–17.

932 64. DasSarma P, Zamora RC, Müller JA, DasSarma S. 2012. Genome-Wide Responses of  
933 the Model Archaeon *Halobacterium* sp. Strain NRC-1 to Oxygen Limitation. J Bacteriol  
934 194:5530–5537.

935 65. Pfeifer F. 2012. Distribution, formation and regulation of gas vesicles. Nat Rev Microbiol  
936 10:705–715.

937 66. Völkner K, Jost A, Pfeifer F. 2020. Accessory Gvp Proteins Form a Complex During Gas  
938 Vesicle Formation of Haloarchaea. Front Microbiol 11.

939 67. Yao AI, Facciotti MT. 2011. Regulatory multidimensionality of gas vesicle biogenesis in  
940 *Halobacterium salinarum* NRC-1. Archaea 2011:716456.

941 68. Bauer M, Marschaus L, Reuff M, Besche V, Sartorius-Neef S, Pfeifer F. 2008.  
942 Overlapping activator sequences determined for two oppositely oriented promoters in  
943 halophilic Archaea. Nucleic Acids Res 36:598–606.

944 69. Scheuch S, Pfeifer F. 2007. GvpD-induced breakdown of the transcriptional activator  
945 GvpE of halophilic archaea requires a functional p-loop and an arginine-rich region of  
946 GvpD. Microbiology (Reading) 153:947–958.

947 70. Schmidt I, Pfeifer F. 2013. Use of GFP-GvpE fusions to quantify the GvpD-mediated  
948 reduction of the transcriptional activator GvpE in haloarchaea. Arch Microbiol 195:403–  
949 412.

950 71. Gelsinger DR, DiRuggiero J. 2018. Transcriptional Landscape and Regulatory Roles of  
951 Small Noncoding RNAs in the Oxidative Stress Response of the Haloarchaeon *Haloferax*  
952 *volcanii*. J Bacteriol 200.

953 72. Morita T, Aiba H. 2019. Mechanism and physiological significance of autoregulation of the  
954 *Escherichia coli* *hfq* gene. RNA 25:264–276.

955 73. Večerek B, Moll I, Bläsi U. 2005. Translational autocontrol of the *Escherichia coli* *hfq* RNA  
956 chaperone gene. RNA 11:976–984.

957 74. Sobrero P, Valverde C. 2011. Evidences of autoregulation of *hfq* expression in  
958 *Sinorhizobium meliloti* strain 2011. *Arch Microbiol* 193:629–639.

959 75. Payá G, Bautista V, Camacho M, Bonete M-J, Esclapez J. 2021. Functional analysis of  
960 Lsm protein under multiple stress conditions in the extreme haloarchaeon *Haloferax*  
961 *mediterranei*. *Biochimie* 187:33–47.

962 76. Desiere F, Deutsch EW, King NL, Nesvizhskii AI, Mallick P, Eng J, Chen S, Eddes J,  
963 Loevenich SN, Aebersold R. 2006. The PeptideAtlas project. *Nucleic Acids Res*  
964 34:D655–D658.

965 77. Van PT, Schmid AK, King NL, Kaur A, Pan M, Whitehead K, Koide T, Facciotti MT, Goo  
966 YA, Deutsch EW, Reiss DJ, Mallick P, Baliga NS. 2008. *Halobacterium salinarum* NRC-1  
967 PeptideAtlas: toward strategies for targeted proteomics and improved proteome  
968 coverage. *J Proteome Res* 7:3755–3764.

969 78. Perez-Riverol Y, Bai J, Bandla C, García-Seisdedos D, Hewapathirana S,  
970 Kamatchinathan S, Kundu DJ, Prakash A, Frericks-Zipper A, Eisenacher M, Walzer M,  
971 Wang S, Brazma A, Vizcaíno JA. 2022. The PRIDE database resources in 2022: a hub  
972 for mass spectrometry-based proteomics evidences. *Nucleic Acids Res* 50:D543–D552.

973 79. Losensky G, Jung K, Urlaub H, Pfeifer F, Fröls S, Lenz C. 2017. Shedding light on biofilm  
974 formation of *Halobacterium salinarum* R1 by SWATH-LC/MS/MS analysis of planktonic  
975 and sessile cells. *Proteomics* 17.

976 80. Völkel S, Hein S, Benker N, Pfeifer F, Lenz C, Losensky G. 2020. How to Cope With  
977 Heavy Metal Ions: Cellular and Proteome-Level Stress Response to Divalent Copper and  
978 Nickel in *Halobacterium salinarum* R1 Planktonic and Biofilm Cells. *Front Microbiol* 10.

979 81. Nagy Z, Chandler M. 2004. Regulation of transposition in bacteria. *Res Microbiol*  
980 155:387–398.

981 82. Altae-Tran H, Kannan S, Demircioglu FE, Oshiro R, Nety SP, McKay LJ, Dlakić M,  
982 Inskeep WP, Makarova KS, Macrae RK, Koonin EV, Zhang F. 2021. The widespread  
983 IS200/605 transposon family encodes diverse programmable RNA-guided  
984 endonucleases. *Science* 0:eabj6856.

985 83. Karvelis T, Druteika G, Bigelyte G, Budre K, Zedaveinyte R, Silanskas A, Kazlauskas D,  
986 Venclovas Č, Siksnys V. 2021. Transposon-associated TnpB is a programmable RNA-  
987 guided DNA endonuclease. *Nature* 1–8.

988 84. Lekontseva N, Mikhailina A, Fando M, Kravchenko O, Balobanov V, Tishchenko S,  
989 Nikulin A. 2020. Crystal structures and RNA-binding properties of Lsm proteins from  
990 archaea *Sulfolobus acidocaldarius* and *Methanococcus vannielii*: Similarity and difference  
991 of the U-binding mode. *Biochimie* 175:1–12.

992 85. Weixlbaumer A, Grünberger F, Werner F, Grohmann D. 2021. Coupling of Transcription  
993 and Translation in Archaea: Cues From the Bacterial World. *Front Microbiol* 12:661827.

994 86. Peck RF, DasSarma S, Krebs MP. 2000. Homologous gene knockout in the archaeon  
995 *Halobacterium salinarum* with *ura3* as a counterselectable marker. *Mol Microbiol* 35:667–  
996 676.

997 87. Bolger AM, Lohse M, Usadel B. 2014. Trimmomatic: a flexible trimmer for Illumina  
998 sequence data. *Bioinformatics* 30:2114–2120.

999 88. Kim D, Paggi JM, Park C, Bennett C, Salzberg SL. 2019. Graph-based genome  
1000 alignment and genotyping with HISAT2 and HISAT-genotype. *Nat Biotechnol* 37:907–  
1001 915.

1002 89. Li H, Handsaker B, Wysoker A, Fennell T, Ruan J, Homer N, Marth G, Abecasis G,  
1003 Durbin R, 1000 Genome Project Data Processing Subgroup. 2009. The Sequence  
1004 Alignment/Map format and SAMtools. *Bioinformatics* 25:2078–2079.

1005 90. Kahles A, Behr J, Rätsch G. 2016. MMR: a tool for read multi-mapper resolution.  
1006 *Bioinformatics* (Oxford, England) 32:770–772.

1007 91. Quinlan AR. 2014. BEDTools: The Swiss-Army Tool for Genome Feature Analysis, p.  
1008 11.12.1-11.12.34. In Bateman, A, Pearson, WR, Stein, LD, Storno, GD, Yates, JR (eds.),  
1009 Current Protocols in Bioinformatics. John Wiley & Sons, Inc., Hoboken, NJ, USA.

1010 92. Wang M, Zhao Y, Zhang B. 2015. Efficient Test and Visualization of Multi-Set  
1011 Intersections. *Sci Rep* 5:16923.

1012 93. Ahlmann-Eltze C, Anders S. 2019. proDA: Probabilistic Dropout Analysis for Identifying  
1013 Differentially Abundant Proteins in Label-Free Mass Spectrometry. *bioRxiv*  
1014 <https://doi.org/10.1101/661496>.

1015 94. Pfeiffer F, Schuster SC, Broicher A, Falb M, Palm P, Rodewald K, Ruepp A, Soppa J,  
1016 Tittor J, Oesterhelt D. 2008. Evolution in the laboratory: the genome of *Halobacterium*  
1017 *salinarum* strain R1 compared to that of strain NRC-1. *Genomics* 91:335–346.

1018 95. Pfeiffer F, Losensky G, Marchfelder A, Habermann B, Dyall-Smith M. 2019. Whole-  
1019 genome comparison between the type strain of *Halobacterium salinarum* (DSM 3754T)  
1020 and the laboratory strains R1 and NRC-1. *Microbiologyopen* 9.

1021 96. Li W, Godzik A. 2006. Cd-hit: a fast program for clustering and comparing large sets of  
1022 protein or nucleotide sequences. *Bioinformatics* 22:1658–1659.

1023 97. Galperin MY, Wolf YI, Makarova KS, Alvarez RV, Landsman D, Koonin EV. 2020. COG  
1024 database update: focus on microbial diversity, model organisms, and widespread  
1025 pathogens. *Nucleic Acids Res* 49:D274–D281.

1026 98. Varani A, Siguier P, Gourbeyre E, Charneau V, Chandler M. 2011. ISsaga is an  
1027 ensemble of web-based methods for high throughput identification and semi-automatic  
1028 annotation of insertion sequences in prokaryotic genomes. *Genome Biol* 12:R30.

1029 99. Bray NL, Pimentel H, Melsted P, Pachter L. 2016. Near-optimal probabilistic RNA-seq  
1030 quantification. *Nat Biotechnol* 34:525–527.

1031 100. Love MI, Huber W, Anders S. 2014. Moderated estimation of fold change and dispersion  
1032 for RNA-seq data with DESeq2. *Genome Biol* 15.

1033 101. Ten-Caten F, Vêncio RZN, Lorenzetti APR, Zaramela LS, Santana AC, Koide T. 2018.  
1034 Internal RNAs overlapping coding sequences can drive the production of alternative  
1035 proteins in archaea. *RNA Biol* 15:1119–1132.

1036 102. Ramírez F, Ryan DP, Grüning B, Bhardwaj V, Kilpert F, Richter AS, Heyne S, Dündar F,  
1037 Manke T. 2016. deepTools2: a next generation web server for deep-sequencing data  
1038 analysis. *Nucleic Acids Res* 44:W160-165.

1039 103. Ritchie ME, Phipson B, Wu D, Hu Y, Law CW, Shi W, Smyth GK. 2015. limma powers  
1040 differential expression analyses for RNA-sequencing and microarray studies. *Nucleic  
1041 Acids Res* 43:e47.

1042 104. Tsirigos KD, Peters C, Shu N, Käll L, Elofsson A. 2015. The TOPCONS web server for  
1043 consensus prediction of membrane protein topology and signal peptides. *Nucleic Acids  
1044 Res* 43:W401-407.

1045 105. Goo YA, Yi EC, Baliga NS, Tao WA, Pan M, Aebersold R, Goodlett DR, Hood L, Ng WV.  
1046 2003. Proteomic analysis of an extreme halophilic archaeon, *Halobacterium* sp. NRC-1.  
1047 *Mol Cell Proteomics* 2:506–524.

1048 106. Klein C, Garcia-Rizo C, Bisle B, Scheffer B, Zischka H, Pfeiffer F, Siedler F, Oesterhelt D.  
1049 2005. The membrane proteome of *Halobacterium salinarum*. *Proteomics* 5:180–197.

1050 107. Wick RR, Judd LM, Holt KE. 2018. Deepbinner: Demultiplexing barcoded Oxford  
1051 Nanopore reads with deep convolutional neural networks. *PLoS Comput Biol*  
1052 14:e1006583.

1053 108. Sedlazeck FJ, Rescheneder P, Smolka M, Fang H, Nattestad M, vonHaeseler A, Schatz  
1054 MC. 2018. Accurate detection of complex structural variations using single-molecule  
1055 sequencing. *Nat Methods* 15:461.

1056 109. Camacho C, Coulouris G, Avagyan V, Ma N, Papadopoulos J, Bealer K, Madden TL.  
1057 2009. BLAST+: architecture and applications. *BMC Bioinformatics* 10:421.

1058 110. Wicker T, Sabot F, Hua-Van A, Bennetzen JL, Capy P, Chalhoub B, Flavell A, Leroy P,  
1059 Morgante M, Panaud O, Paux E, SanMiguel P, Schulman AH. 2007. A unified  
1060 classification system for eukaryotic transposable elements. *Nat Rev Genet* 8:973–982.

1061 111. Sharp PM, Li WH. 1987. The codon Adaptation Index — a measure of directional  
1062 synonymous codon usage bias, and its potential applications. *Nucleic Acids Res*  
1063 15:1281–1295.

1064 112. Gu Z, Hübschmann D. 2021. Make Interactive Complex Heatmaps in R. *Bioinformatics*  
1065 btab806.

1066 113. Gu Z, Eils R, Schlesner M. 2016. Complex heatmaps reveal patterns and correlations in  
1067 multidimensional genomic data. *Bioinformatics* 32:2847–2849.

1068 114. Robinson JT, Thorvaldsdóttir H, Turner D, Mesirov JP. 2020. igv.js: an embeddable  
1069 JavaScript implementation of the Integrative Genomics Viewer (IGV). *bioRxiv*  
1070 <https://doi.org/10.1101/2020.05.03.075499>.

1071

1072

1073 **FIGURES**

1074 Figure 1 | Features potentially associated with post-transcriptional regulation. Four features  
1075 related to the post-transcriptional regulation in *H. salinarum*. Sets are comprised of genes that  
1076 bind to SmAP1, show transcript processing sites (TPS), have a putative cis-regulatory antisense  
1077 RNA (asRNA), and are differentially expressed in the RNase\_2099C knockout strain  
1078 ( $\Delta VNG\_2099C$ ).

1079 Figure 2 | Genes following patterns compatible with post-transcriptional regulation. Each panel  
1080 shows protein (y-axis) and mRNA (x-axis) absolute abundance ( $\log_{10}$ -transformed) or relative  
1081 changes ( $\log_2$  fold change). Absolute abundance-based analysis is reported from **A** to **D** in a time  
1082 point-wise manner and from **E** to **G** in a time-lag perspective. Gray points represent entities  
1083 following usual patterns; orange points represent entities within the upper quintile of protein  
1084 abundance and lower quintile of mRNA abundance; green points represent entities within the  
1085 lower quintile of protein abundance and upper quintile of mRNA abundance. The solid black line  
1086 illustrates the fitted linear regression model. **H**, **I**, and **J** present the relative abundance-based  
1087 analysis of protein and mRNA levels in consecutive physiological state transitions. **K** and **L**  
1088 present the same variables for long physiological state transitions. Points are color-coded  
1089 according to multiple combinations of change status considering both variables. TP1: early  
1090 exponential growth phase; TP2: mid-exponential growth phase; TP3: late exponential growth  
1091 phase; TP4: stationary phase.

1092 Figure 3 | An atlas of the transcriptome, ribosome profile, and proteome for *Halobacterium*  
1093 *salinarum* NRC-1. The heatmap shows quantile-normalized  $\log_{10}$ -transformed abundance levels  
1094 for proteins (a pseudocount was imputed for missing values), messenger RNAs (mRNAs;  
1095 TPM+1), and ribosome-protected mRNA fragments (RPF; TPM+1) for 2,579 genes across four  
1096 consecutive stages of batch culture growth, namely early exponential, mid-exponential, late  
1097 exponential, and stationary phase (TP1, TP2, TP3, and TP4, respectively).  $\log_2$ -transformed  
1098 translational efficiency (TE) and ribosome occupancy (RO) were computed by dividing protein  
1099 levels by mRNA levels and mRNA levels by RPF levels, respectively. We present general features  
1100 on the left-hand side, starting with the cluster of orthologous genes (COG) functional categories  
1101 (97), split into groups before clustering the protein levels. Chromosome, pNRC100, and pNRC200  
1102 show the replicon location of each gene within the genome. The presence of SmAP1 binding,  
1103 antisense RNAs (asRNA) (46), and putative endoribonuclease-generated transcript processing  
1104 sites (TPS) (47) are indicated in corresponding tracks. The 2099 track shows  $\log_2$  fold change  
1105 (LFC) of transcript levels in the RNase\_2099C null mutant ( $\Delta VNG\_2099C$ ) relative to the parent

1106  $\Delta ura3$  strain (21). mRNA half-lives (43), codon adaptation index (CAI), and the deviation of GC  
1107 content from average GC content of all transcripts are also indicated in corresponding tracks. See  
1108 inset keys for color codes for each track and Methods section for details. Interactive and expanded  
1109 static versions of this figure are available in our *H. salinarum* NRC-1 multi-omics Atlas portal  
1110 (<https://halodata.systemsbiology.net>).

1111 Figure 4 | Functions of putative post-transcriptionally regulated genes and potential driving  
1112 mechanisms. The figure shows the common properties of groups of putative post-transcriptionally  
1113 regulated genes. **A.** The union set of genes found by the absolute abundance-based approach  
1114 across the growth curve (green points in Figure 2A-D). **B-E.** Arbitrarily selected genes of known  
1115 functions (subsets of **A**). **F-H.** Gene categories according to clusters of orthologous genes (COG)  
1116 with enriched features compatible with the post-transcriptional regulation hypothesis (subsets of  
1117 **A**). **I.** The union set of genes found by the relative abundance-based approach across the growth  
1118 curve (upregulated mRNA and downregulated protein; green clusters in Figure 2H-L). **J.** Genes  
1119 of the *gvp* cluster in the transition from early exponential (TP1) to mid-exponential growth phase  
1120 (TP2) (subset of **I**). See File S4 for a complete list of genes within each group (**A, F-H, I**) and the  
1121 respective supporting evidence. TPS: Transcript processing sites; asRNA: antisense RNA; CAI:  
1122 Codon adaptation index.

1123 Figure 5 | Protein and mRNA levels of mobile genetic elements. **A.** Log<sub>10</sub>-transformed expression  
1124 profile of proteins (a pseudocount was imputed for missing values), mRNAs (TPM+1), and  
1125 ribosome-protected mRNA fragments (RPF; TPM+1) with miscellaneous properties of genes  
1126 classified by clusters of orthologous genes (COG) within the “Mobilome: prophages, transposons”  
1127 category (pink). TE: translational efficiency; RO: ribosome occupancy; asRNAs: antisense RNA;  
1128 TPS: transcript processing site; 2099: log<sub>2</sub> fold change (LFC) of transcripts in the absence of  
1129 RNase\_2099C; TP1: early exponential growth phase; TP2: mid-exponential growth phase; TP3:  
1130 late exponential growth phase; TP4: stationary phase. Box plots aid the comparison between  
1131 features of genes within the “Mobilome: prophages, transposons” versus the pool of the other  
1132 categories: **B.** GC content; **C.** Log<sub>10</sub>-transformed average protein abundance across all time  
1133 points (missing values excluded); **D.** Codon adaptation index (CAI). **E.** Log<sub>10</sub>-transformed average  
1134 mRNA levels (TPM+1) across all time points. We compared medians using the Mann–Whitney U  
1135 test. \* *p*-value  $\leq 5 \times 10^{-2}$ ; \*\* *p*-value  $\leq 10^{-2}$ ; \*\*\*\* *p*-value  $\leq 10^{-4}$ .

1136 Figure 6 | Detected mobilizations for decomposed insertion sequence families. The figure shows  
1137 the average normalized number of clusters for each strain. The panels, from top to bottom, show

1138 the results for the **(A)** pool of all insertion sequences, **(B)** IS4 family only, **(C)** ISH3 family only,  
1139 and **(D)** the other families. Black lines indicate the range of the 68% confidence interval.

1140 Figure 7 | Post-transcriptional regulation of *gvp* operons. **A.** Arrows represent how each one of  
1141 the gas vesicle operon genes (color-coded; protein names in parentheses) behaves regarding its  
1142  $\log_2$ -transformed protein abundance (y-axis) and mRNA abundance (x-axis) across consecutive  
1143 physiological states (TP1: early exponential growth phase; TP2: mid-exponential growth phase;  
1144 TP3: late exponential growth phase; TP4: stationary phase). We represent *gvpMLKJIHGFED* and  
1145 *gvpACNO* operons, except for a few elements (*gvpG*, *gvpl*, *gvpK*, and *gvpM*), whose protein  
1146 levels were not detected by our SWATH-MS approach. **B.** The genome browser snapshot reveals  
1147 the region of *gvpDEFGHIJKLM* (reverse strand) and *gvpACNO* (forward strand)  
1148 (NC\_001869.1:16,000-25,500). We depict genes as blue rectangles. Tracks show various  
1149 features described on the left-hand side of the panel. Green ticks represent transcript processing  
1150 sites (TPS); red rectangles represent SmAP1 binding sites; purple rectangles represent annotated  
1151 antisense RNAs. **C.** Time point-wise regulatory scheme of gas vesicles proteins encoded by the  
1152 *gvp* cluster. Blue bars represent translational repression, red arrows represent transcriptional  
1153 activation, and green bars represent post-translational degradation. Protein abundance is  
1154 depicted by the font size of gas vesicle proteins (GvpX).

1155 **SUPPLEMENTAL TABLES**

1156 Table S1 | Annotation sources for constructing the *Halobacterium salinarum* NRC-1 non-  
1157 redundant transcriptome and a loci dictionary.

1158 Table S2 | Comparison of Pearson correlation coefficient computed for protein and mRNA  
1159 abundance throughout the growth curve. We compared the coefficients using Zou's confidence  
1160 interval method implemented in the cocor package. Subscripts *P* and *m* refer to protein and mRNA  
1161 levels for indicated time points. Uppercase letters (A-F) refer to panels in Figure 2. \*  $\Delta R$  stands  
1162 for the subtraction between the two coefficients (e.g.,  $R_{TP1(A)} - R_{TP2(B)}$ ). A confidence interval (CI)  
1163 of  $\Delta R$  spanning zero is not significant. Coefficients diverge slightly from those presented in the  
1164 main text due to technical differences between the comparative approach and classic correlation  
1165 method implementations. TP1: early exponential growth phase; TP2: mid-exponential growth  
1166 phase; TP3: late exponential growth phase; TP4: stationary phase.

1167 Table S3 | The non-redundant set of insertion sequences in *Halobacterium salinarum* NRC-1. We  
1168 obtained insertion sequence families from ISfinder and ISsaga, and the transposition mechanisms  
1169 from Siguier et al. (2015).

1170 Table S4 | Summary of the transposition detection assay. <sup>a</sup> Number of identified insertion clusters.  
1171 <sup>b</sup> Number of identified excision clusters. <sup>c</sup> Number of reads aligned to the reference genome. <sup>d</sup>  
1172 Sum of insertion and excision clusters normalized by the library with the highest number of aligned  
1173 reads.

1174 Table S5 | List of primers used in this study.

1175 Table S6 | In-house and third-party GitHub repositories cited in this study.

1176

1177 **SUPPLEMENTAL FIGURES**

1178 Figure S1 | Quality assurance of co-immunoprecipitated samples. **A.** Western blot of samples  
1179 extracted from strains expressing plasmids for cMyc and cMyc-tagged SmAP1 (see lane titles for  
1180 labels). The expected molecular weight of the cMyc-tagged SmAP1 complex is 37 kDa. BR:  
1181 Biological replicate. **B.** Polymerase Chain Reaction (PCR) of RNA-purified samples treated with  
1182 DNase. M: Ladder; 1: Positive control (genomic DNA amplified using 19-fwd and 20-rev primers  
1183 with a predicted amplicon size of 85 bp); 2-5: cMyc BR1, cMyc BR2, SmAP1-cMyc BR1, and  
1184 SmAP1-cMyc BR2 (amplified using 19-fwd and 20-rev primers); 6: Positive control (genomic DNA  
1185 amplified using 63-fwd and 64-rev primers with a predicted amplicon size of 450 bp). 7-10: cMyc  
1186 BR1, cMyc BR2, SmAP1-cMyc BR1, and SmAP1-cMyc BR2 (amplified using 63-fwd and 64-rev  
1187 primers).

1188 Figure S2 | SmAP1 features. **A.** SmAP1 binding is conditioned to the GC content of transcripts.  
1189 The reduced GC content of transcripts is a property influencing SmAP1 binding. We compared  
1190 medians using the Mann–Whitney U test. \*\*\*\*  $p$ -value  $\leq 10^{-4}$ . **B.** Time course view of protein,  
1191 ribosome-protected mRNA fragments (RPF; TPM+1), and mRNA levels (TPM+1). Vertical bars  
1192 represent the standard error computed using at least six replicates for proteins and three  
1193 replicates for mRNA and RPF. **C.** Functional categories of transcripts bound to SmAP1. The panel  
1194 shows how many genes have transcripts bound to SmAP1, considering each category of COG  
1195 (clusters of orthologous genes). The left-hand side panel shows categories with no more than 25  
1196 genes with SmAP1-bound transcripts, and the right-hand side panel shows genes within the  
1197 “Function unknown” category. We highlighted enriched categories with an asterisk (\*  $p$ -value <  
1198 0.05).

1199 Figure S3 | Venn diagrams of putative post-transcriptionally regulated genes shared among  
1200 different physiological states. **A.** Entities with proteins within the lower quintile of protein levels or  
1201 not detected by our proteome survey whose mRNA levels are within the upper quintile (union set  
1202 = 167). **B.** Entities within the lower quintile of protein levels and within the upper quintile of mRNA  
1203 levels (union set = 64). **C.** Entities with proteins not detected by our proteome survey and within  
1204 the upper quintile of mRNA levels (union set = 117). TP1: early exponential growth phase; TP2:  
1205 mid-exponential growth phase; TP3: late exponential growth phase; TP4: stationary phase. All  
1206 sets are available in File S3.

1207 Figure S4 | Atlas section of putative post-transcriptionally regulated genes in the transition from  
1208 TP1 to TP2. This section of the atlas shows genes having downregulated proteins and  
1209 upregulated mRNAs (green cluster in Figure 2H) in the transition from the early exponential

1210 growth phase (TP1) to mid-exponential growth phase (TP2). The heatmap represents  $\log_{10}$ -  
1211 transformed expression profile of proteins (a pseudocount was imputed for missing values),  
1212 mRNAs (TPM+1), and ribosome-protected mRNA fragments (RPF; TPM+1). Heatmaps also  
1213 represent the respective  $\log_2$ -transformed translational efficiency (TE) and ribosome occupancy  
1214 (RO) for each time point. COG: clusters of orthologous genes; asRNAs: antisense RNA; TPS:  
1215 transcript processing site; 2099:  $\log_2$  fold change (LFC) of transcripts in the absence of  
1216 RNase\_2099C; CAI: codon adaptation index; TP3: late exponential growth phase; TP4: stationary  
1217 phase.

1218 Figure S5 | UpSet plot of putative post-transcriptionally regulated genes shared in different  
1219 physiological state transitions. Entities being downregulated at the protein level and upregulated  
1220 at the mRNA level (union set = 26). TP1: early exponential growth phase; TP2: mid-exponential  
1221 growth phase; TP3: late exponential growth phase; TP4: stationary phase. All sets are available  
1222 in File S6.

1223 Figure S6 | Protein levels are associated with transcript GC content. The solid line illustrates the  
1224 locally weighted smoothing (loess), and the shaded gray ribbon indicates its 95% confidence  
1225 interval. A dashed line indicates the average GC content computed using the whole set of  
1226 transcripts. Points follow a color gradient defined by the codon adaptation index (CAI). TP1: early  
1227 exponential growth phase; TP2: mid-exponential growth phase; TP3: late exponential growth  
1228 phase; TP4: stationary phase.

1229 Figure S7 | VNG\_0112H, a transposase encoded by the ISH3B element. Tracks show various  
1230 features described on the left-hand side of the panel. Green tick marks represent transcript  
1231 processing sites (TPS); red rectangles represent SmAP1 binding sites; a blue rectangle (reverse  
1232 strand) represents the open reading frame for the transposase VNG\_0112H; a green rectangle  
1233 (reverse strand) represent the ISH3B element. Gray single-nucleotide resolution bar plots  
1234 represent RNA-Seq and Ribo-Seq coverage; TP2: mid-exponential growth phase.

1235 Figure S8 | Detected mobilization events. **A.** Detected insertions. **B.** Detected excisions.  
1236 Observed events are the number of detected clusters for each type of mobilization. All the cluster  
1237 types are represented, considering those classified as predominant, common, and rare. Bars are  
1238 color-coded according to insertion sequence families.

1239 Figure S9 | Protein-mRNA dynamics and various features of genes encoding gas vesicle  
1240 biogenesis proteins. We represented the 14 genes comprising the *gvpDEFGHIJKLM* and  
1241 *gvpACNO* operons in the context of their features. SmAP1 binding, antisense RNAs (asRNAs),

1242 and transcript processing sites (TPS) are enriched in this cluster ( $p$ -value =  $2.4 \times 10^{-7}$ ,  $3 \times 10^{-3}$ , and  
1243  $3.8 \times 10^{-2}$ , respectively). The heatmap represents  $\log_{10}$ -transformed expression profile of proteins  
1244 (a pseudocount was imputed for missing values), mRNAs (TPM+1), and ribosome-protected  
1245 mRNA fragments (RPF; TPM+1). Heatmaps also represent the respective  $\log_2$ -transformed  
1246 translational efficiency (TE) and ribosome occupancy (RO) for each time point. COG: clusters of  
1247 orthologous genes; 2099:  $\log_2$  fold change (LFC) of transcripts in the absence of RNase\_2099C;  
1248 CAI: codon adaptation index; TP1: early exponential growth phase; TP2: mid-exponential growth  
1249 phase; TP3: late exponential growth phase; TP4: stationary phase.

1250 Figure S10 | *gvpACN* loci reveal differential patterns of Ribo-Seq signal. We present the three  
1251 consecutive loci (VNG\_7025-VNG\_7027) comprising the *gvpACN* region (blue rectangles). The  
1252 time point-wise Ribo-Seq and RNA-Seq normalized profiles are represented by gray bars. Red  
1253 rectangles represent SmAP1 binding sites; green tick marks represent transcript processing sites  
1254 (TPS); purple rectangles represent antisense RNAs. Each track was automatically scaled using  
1255 the “Autoscale” feature of Integrative Genomics Viewer. We observe that pile-ups of Ribo-Seq  
1256 emerge after the late exponential growth phase (TP3), indicating that the elongation phase of  
1257 translation intensifies late on growth. Concurrently, we see SmAP1 binding sites either right  
1258 before or spanning the region where the peaks emerge, indicating the role of this protein as a  
1259 translational regulator. TP1: early exponential growth phase; TP2: mid-exponential growth phase;  
1260 TP4: stationary phase.

1261 Figure S11 | VNG\_0042G, a TnpB encoded by the ISH39 element from the IS200/IS605 family  
1262 subgroup IS1341. Tracks show various features described on the left-hand side of the panel.  
1263 Green tick marks represent transcript processing sites (TPS); red rectangles represent SmAP1  
1264 binding sites; a purple rectangle (forward strand) represent an annotated antisense RNA; a blue  
1265 rectangle (reverse strand) represents the open reading frame for TnpB; a green rectangle  
1266 (reverse strand) represents the ISH39 element. Gray single-nucleotide resolution bar plots  
1267 represent RNA-Seq and Ribo-Seq coverage; TP2: mid-exponential growth phase.

1268 Figure S12 | Growth curve of  $\Delta$ ura3 and  $\Delta$ ura3 $\Delta$ smap1 strains. We conducted a growth curve  
1269 experiment with three biological replicates for  $\Delta$ ura3 (blue lines) and  $\Delta$ ura3 $\Delta$ smap1 (orange lines)  
1270 strains. Line types depict each of the biological replicates.

1271 **SUPPLEMENTAL FILES**

1272 File S1 | Atlas data. The non-redundant transcriptome locus tag dictionary, the normalized atlas  
1273 data, and the non-normalized atlas data.

1274 File S2 | Differentially expressed genes in the absence of RNase\_2099C.

1275 File S3 | Putative post-transcriptionally regulated genes (absolute abundance-based approach).  
1276 Genes with patterns compatible with the post-transcriptional regulation hypothesis found by the  
1277 abundance-based approach.

1278 File S4 | Gene set enrichment analysis and comparison of features. Comparison of quantitative  
1279 variables and enrichment tests for putative post-transcriptionally regulated gene sets found by the  
1280 absolute abundance- and by the relative abundance-based approaches.

1281 File S5 | Differential expression analysis of transcripts and proteins across the growth curve.

1282 File S6 | Putative post-transcriptionally regulated genes (relative abundance-based approach).  
1283 Genes with patterns compatible with the post-transcriptional regulation hypothesis found by the  
1284 relative abundance -based approach.

1285 File S7 | Atlas heatmap (expanded version). This file brings an expanded version of Figure 3.

1286 File S8 | Insertion sequence mobilization events detected by the long-read DNA-Seq experiment.

## FIGURES

### Title: A genome-scale atlas reveals complex interplay of transcription and translation in an archaeon

Authors: Alan P. R. Lorenzetti <sup>1,2</sup>, Ulrike Kusebauch <sup>2</sup>, Lívia S. Zaramela <sup>1</sup>, Wei-Ju Wu <sup>2</sup>, João P. P. de Almeida <sup>1,3</sup>, Serdar Turkarslan <sup>2</sup>, Adrián L. G. de Lomana <sup>2,4</sup>, José V. Gomes-Filho <sup>1,5</sup>, Ricardo Z. N. Vêncio <sup>6</sup>, Robert L. Moritz <sup>2</sup>, Tie Koide <sup>1,†</sup>, Nitin S. Baliga <sup>2,7,8,9,†,#</sup>

#### Affiliations:

<sup>1</sup> Department of Biochemistry and Immunology, Ribeirão Preto Medical School, University of São Paulo, Ribeirão Preto, Brazil

<sup>2</sup> Institute for Systems Biology, Seattle, WA, USA

<sup>3</sup> Present address: Institute of Biological Sciences, Federal University of Minas Gerais, Belo Horizonte, Brazil

<sup>4</sup> Present address: Center for Systems Biology, University of Iceland, Reykjavik, Iceland

<sup>5</sup> Present address: Prokaryotic RNA Biology, Phillips-Universität Marburg, Marburg, Germany

<sup>6</sup> Department of Computation and Mathematics, Faculty of Philosophy, Sciences and Letters at Ribeirão Preto, University of São Paulo, Ribeirão Preto, Brazil

<sup>7</sup> Departments of Biology and Microbiology, University of Washington, Seattle, WA, USA

<sup>8</sup> Molecular and Cellular Biology Program, University of Washington, Seattle, WA, USA

<sup>9</sup> Lawrence Berkeley National Lab, Berkeley, CA, USA

† TK and NSB are joint senior authors

# Author to whom correspondence should be addressed

E-mail: nitin.baliga@isbscience.org; Tel.: +1 (206) 732-1266

Feature	Number of Genes
SmAP1	397
TPS	966
1	561
2-5	380
>5	25
asRNA	536
$\Delta RNase\_2099C$	166
Upregulated	82
Downregulated	84

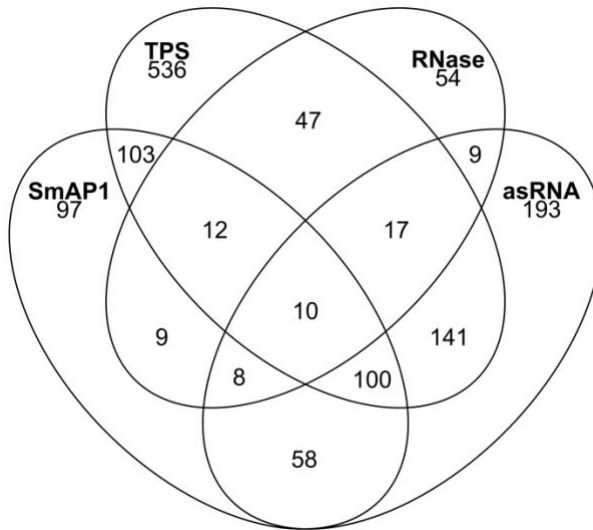


**Figure 1 | Features potentially associated with post-transcriptional regulation.** Four features related to the post-transcriptional regulation in *H. salinarum*. Sets are comprised of genes that bind to SmAP1, show transcript processing sites (TPS), have a putative cis-regulatory antisense RNA (asRNA), and are differentially expressed in the RNase\_2099C knockout strain ( $\Delta VNG\_2099C$ ).

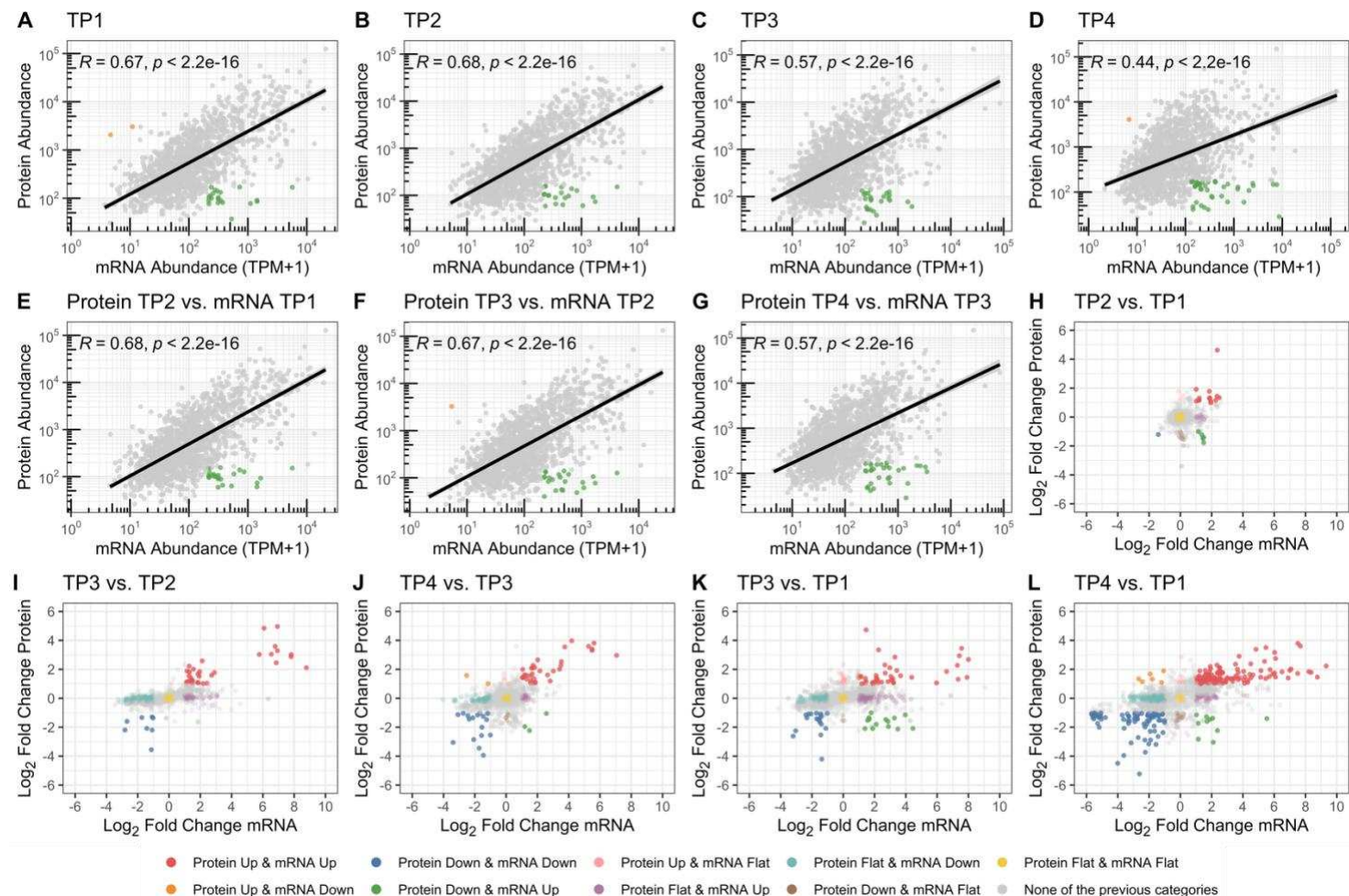


**Figure 2 | Genes following patterns compatible with post-transcriptional regulation.** Each panel shows protein (y-axis) and mRNA (x-axis) absolute abundance ( $\log_{10}$ -transformed) or relative changes ( $\log_2$  fold change). Absolute abundance-based analysis is reported from **A** to **D** in a time point-wise manner and from **E** to **G** in a time-lag perspective. Gray points represent entities following usual patterns; orange points represent entities within the upper quintile of protein abundance and lower quintile of mRNA abundance; green points represent entities within the lower quintile of protein abundance and upper quintile of mRNA abundance. The solid black line illustrates the fitted linear regression model. **H**, **I**, and **J** present the relative abundance-based analysis of protein and mRNA levels in consecutive physiological state transitions. **K** and **L** present the same variables for long physiological state transitions. Points are color-coded according to multiple combinations of change status considering both variables. TP1: early exponential growth phase; TP2: mid-exponential growth phase; TP3: late exponential growth phase; TP4: stationary phase.

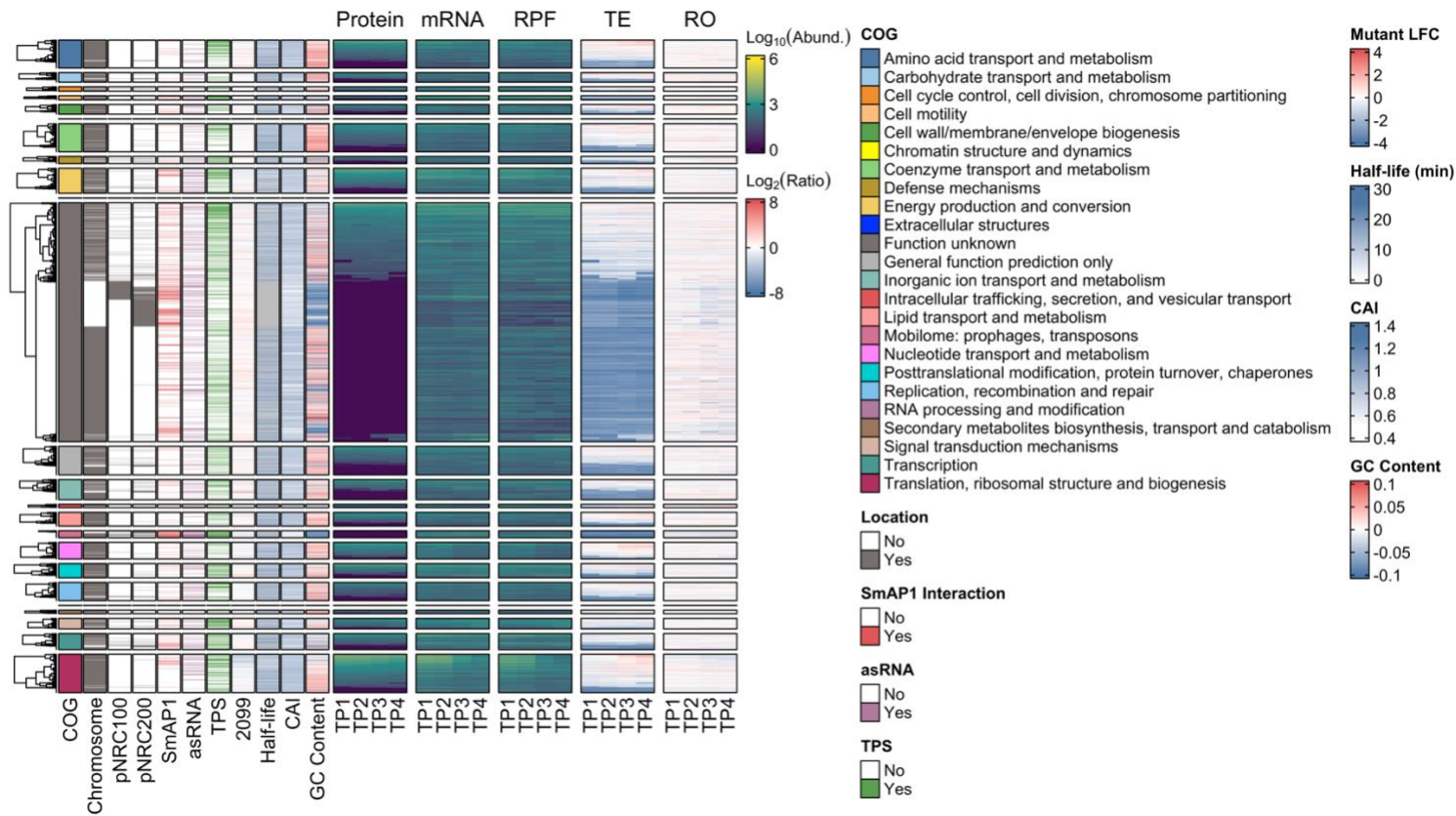


**Figure 3 | An atlas of the transcriptome, ribosome profile, and proteome for *Halobacterium salinarum* NRC-1.** The heatmap shows quantile-normalized log<sub>10</sub>-transformed abundance levels for proteins (a pseudocount was imputed for missing values), messenger RNAs (mRNAs; TPM+1), and ribosome-protected mRNA fragments (RPF; TPM+1) for 2,579 genes across four consecutive stages of batch culture growth, namely early exponential, mid-exponential, late exponential, and stationary phase (TP1, TP2, TP3, and TP4, respectively). Log<sub>2</sub>-transformed translational efficiency (TE) and ribosome occupancy (RO) were computed by dividing protein levels by mRNA levels and mRNA levels by RPF levels, respectively. We present general features on the left-hand side, starting with the cluster of orthologous genes (COG) functional categories (97), split into groups before clustering the protein levels. Chromosome, pNRC100, and pNRC200 show the replicon location of each gene within the genome. The presence of SmAP1 binding, antisense RNAs (asRNA) (46), and putative endoribonuclease-generated transcript processing sites (TPS) (47) are indicated in corresponding tracks. The 2099 track shows log<sub>2</sub> fold change (LFC) of transcript levels in the RNase\_2099C null mutant ( $\Delta$ VNG\_2099C) relative to the parent  $\Delta$ ura3 strain (21). mRNA half-lives (43), codon adaptation index (CAI), and the deviation of GC content from average GC content of all transcripts are also indicated in corresponding tracks. See inset keys for color codes for each track and Methods section for details. Interactive and expanded static versions of this figure are available in our *H. salinarum* NRC-1 multi-omics Atlas portal (<https://halodata.systemsbiology.net>).

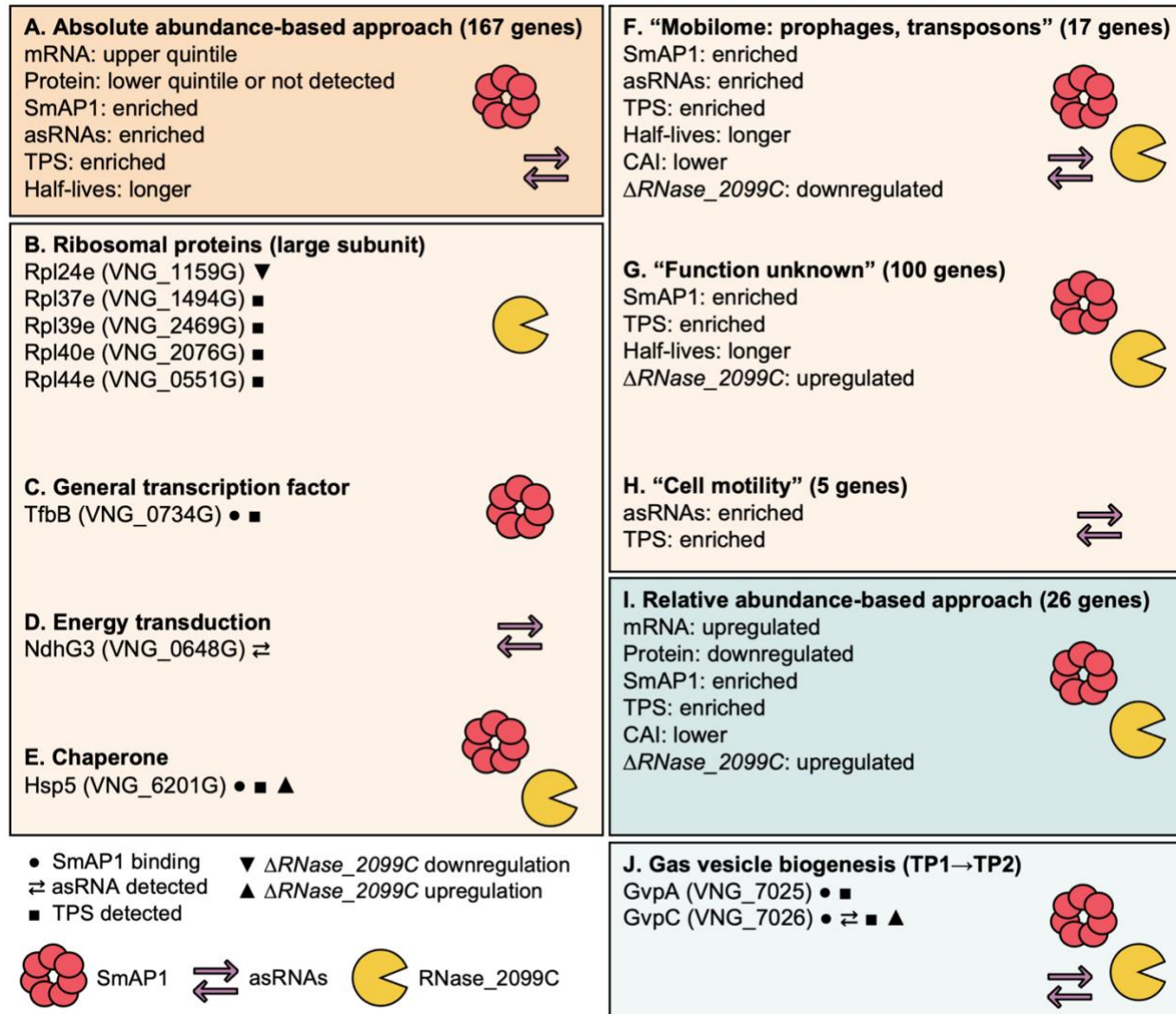


**Figure 4 | Functions of putative post-transcriptionally regulated genes and potential driving mechanisms.** The figure shows the common properties of groups of putative post-transcriptionally regulated genes. **A.** The union set of genes found by the absolute abundance-based approach across the growth curve (green points in Figure 2A-D). **B-E.** Arbitrarily selected genes of known functions (subsets of A). **F-H.** Gene categories according to clusters of orthologous genes (COG) with enriched features compatible with the post-transcriptional regulation hypothesis (subsets of A). **I.** The union set of genes found by the relative abundance-based approach across the growth curve (upregulated mRNA and downregulated protein; green clusters in Figure 2H-L). **J.** Genes of the *gvp* cluster in the transition from early exponential (TP1) to mid-exponential growth phase (TP2) (subset of I). See File S4 for a complete list of genes within each group (A, F-H, I) and the respective supporting evidence. TPS: Transcript processing sites; asRNA: antisense RNA; CAI: Codon adaptation index.

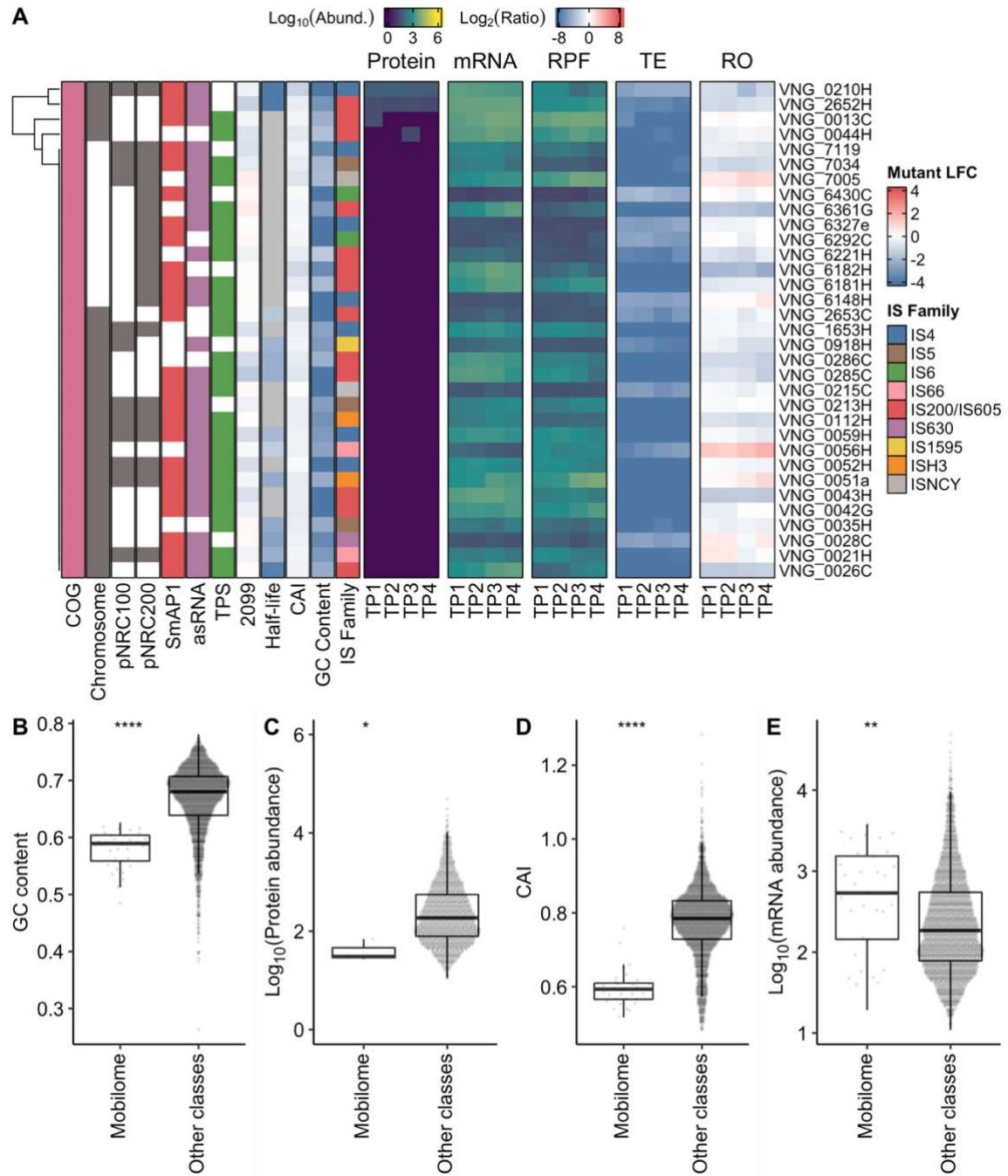


**Figure 5 | Protein and mRNA levels of mobile genetic elements. A.**  $\text{Log}_{10}$ -transformed expression profile of proteins (a pseudocount was imputed for missing values), mRNAs (TPM+1), and ribosome-protected mRNA fragments (RPF; TPM+1) with miscellaneous properties of genes classified by clusters of orthologous genes (COG) within the “Mobilome: prophages, transposons” category (pink). TE: translational efficiency; RO: ribosome occupancy; asRNAs: antisense RNA; TPS: transcript processing site; 2099:  $\log_2$  fold change (LFC) of transcripts in the absence of RNase\_2099C; TP1: early exponential growth phase; TP2: mid-exponential growth phase; TP3: late exponential growth phase; TP4: stationary phase. Box plots aid the comparison between features of genes within the “Mobilome: prophages, transposons” versus the pool of the other categories: **B.** GC content; **C.**  $\text{Log}_{10}$ -transformed average protein abundance across all time points (missing values excluded); **D.** Codon adaptation index (CAI). **E.**  $\text{Log}_{10}$ -transformed average mRNA levels (TPM+1) across all time points. We compared medians using the Mann–Whitney U test. \*  $p$ -value  $\leq 5 \times 10^{-2}$ ; \*\*  $p$ -value  $\leq 10^{-2}$ ; \*\*\*\*  $p$ -value  $\leq 10^{-4}$ .

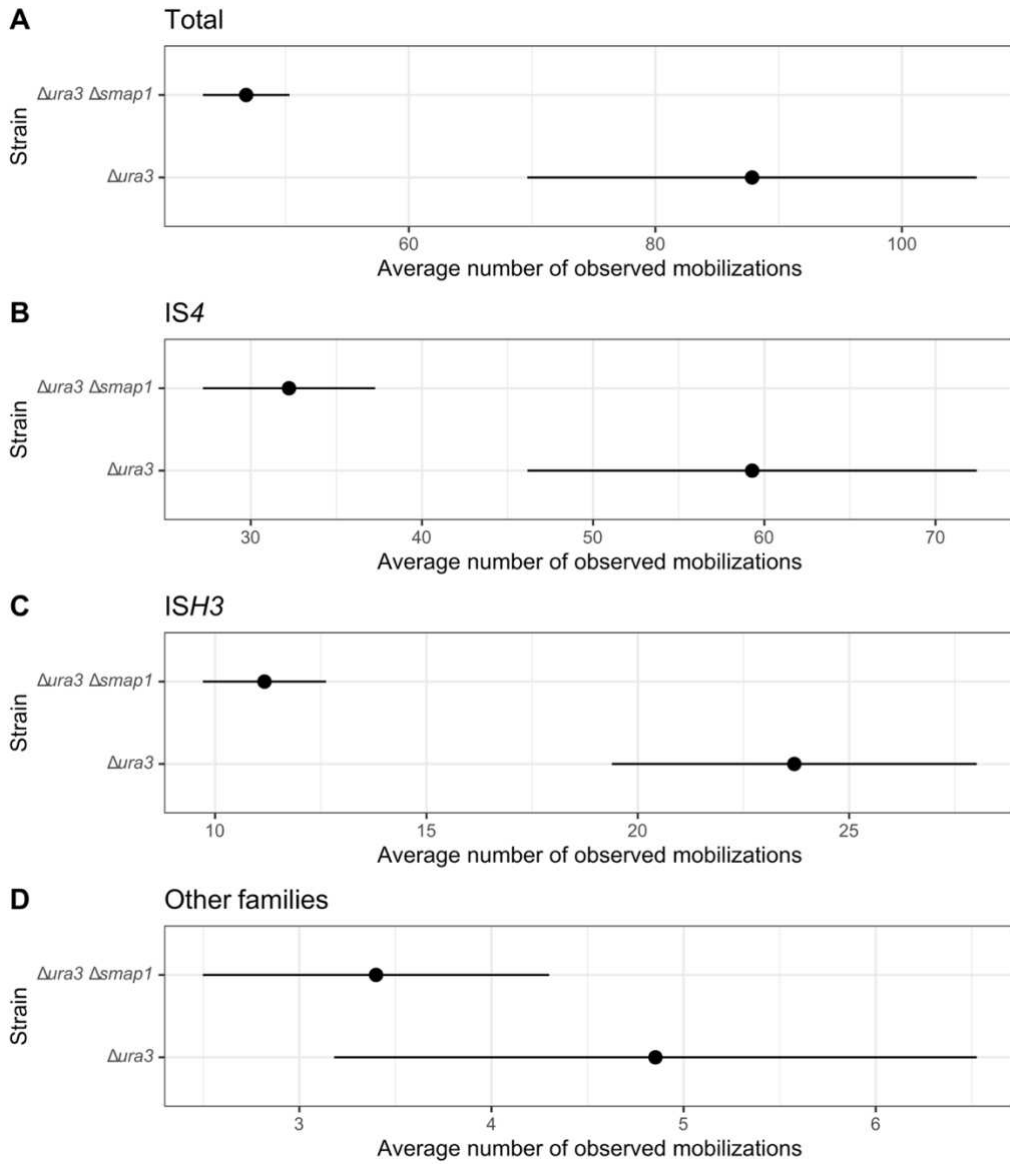


**Figure 6 | Detected mobilizations for decomposed insertion sequence families.** The figure shows the average normalized number of clusters for each strain. The panels, from top to bottom, show the results for the (A) pool of all insertion sequences, (B) IS4 family only, (C) ISH3 family only, and (D) the other families. Black lines indicate the range of the 68% confidence interval.

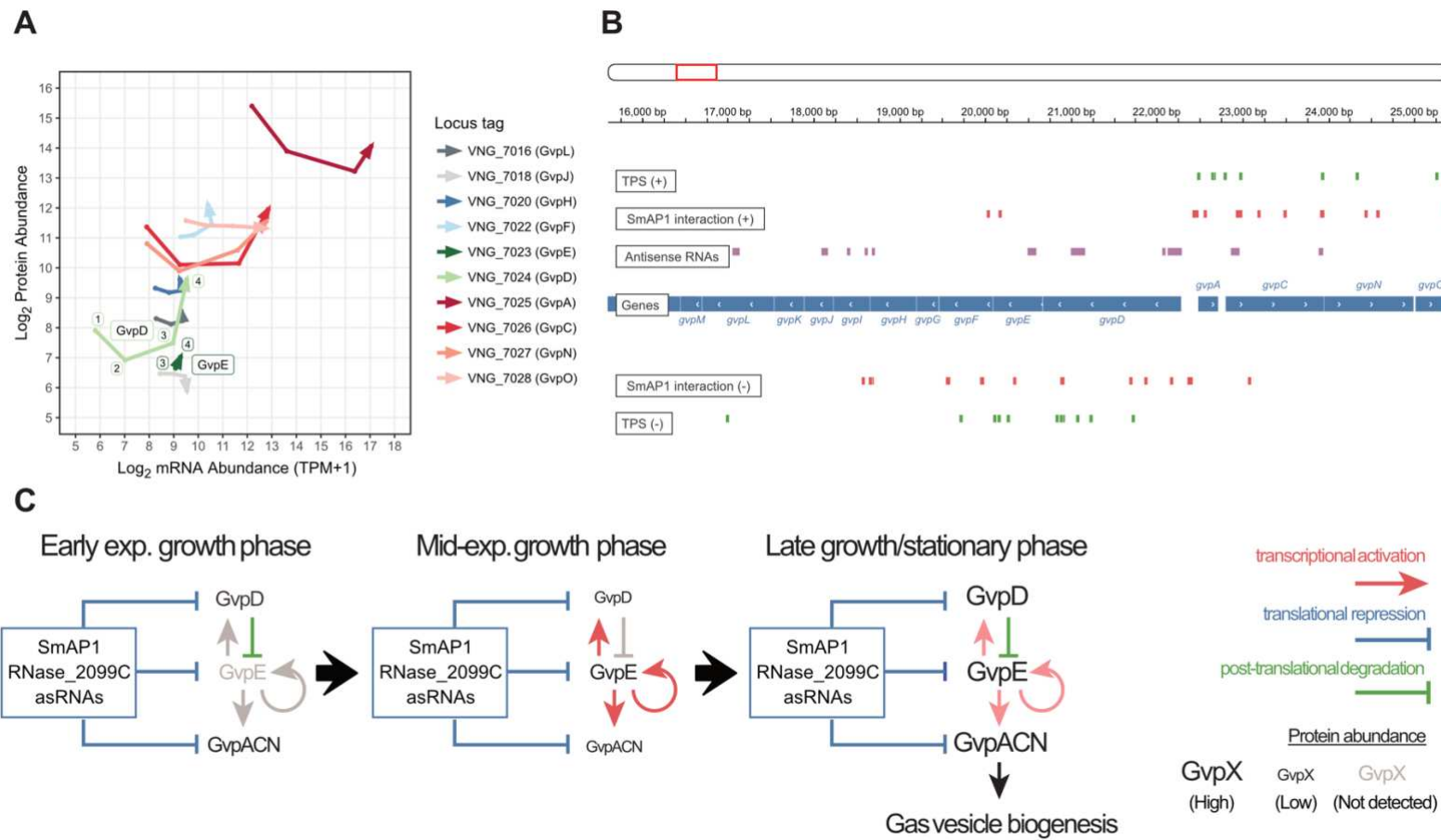


**Figure 7 | Post-transcriptional regulation of *gvp* operons. A.** Arrows represent how each one of the gas vesicle operon genes (color-coded; protein names in parentheses) behaves regarding its log<sub>2</sub>-transformed protein abundance (y-axis) and mRNA abundance (x-axis) across consecutive physiological states (TP1: early exponential growth phase; TP2: mid-exponential growth phase; TP3: late exponential growth phase; TP4: stationary phase). We represent *gvpMLKJHGFED* and *gvpACNO* operons, except for a few elements (*gvpG*, *gvpI*, *gvpK*, and *gvpM*), whose protein levels were not detected by our SWATH-MS approach. **B.** The genome browser snapshot reveals the region of *gvpDEFGHJKLM* (reverse strand) and *gvpACNO* (forward strand) (NC\_001869.1:16,000-25,500). We depict genes as blue rectangles. Tracks show various features described on the left-hand side of the panel. Green ticks represent transcript processing sites (TPS); red rectangles represent SmAP1 binding sites; purple rectangles represent annotated antisense RNAs. **C.** Time point-wise regulatory scheme of gas vesicles proteins encoded by the *gvp* cluster. Blue bars represent translational repression, red arrows represent transcriptional activation, and green bars represent post-translational degradation. Protein abundance is depicted by the font size of gas vesicle proteins (GvpX).